Numerical study of the dam-break waves and Favre waves down sloped wet rigid-bed at laboratory scale

Numerical study of the dam-break waves and Favre waves down sloped wet rigid-bed at laboratory scale

Wenjun Liu[1], Bo Wang[2], Yakun Guo[3]

[1]PhD student, State Key Laboratory of Hydraulics and Mountain River Engineering, College of Water Resource and Hydropower, Sichuan University, Chengdu, 610065, China. E-mail: liuwenjun_scu@163.com

[2]Professor, State Key Laboratory of Hydraulics and Mountain River Engineering, Sichuan University, College of Water Resource and Hydropower, Chengdu, 610065, China. ORCID: https://orcid.org/0000-0002-9027-4077. E-mail: wangbo@scu.edu.cn(Corresponding author)

[3]Professor, Faculty of Engineering & Informatics, University of Bradford, BD7 1DP, UK. E-mail: y.guo16@bradford.ac.uk

Abstract: The bed slope and the tailwater depth are two important ones among the factors that affect the propagation of the dam-break flood and Favre waves. Most previous studies have only focused on the macroscopic characteristics of the dam-break flows or Favre waves under the condition of horizontal bed, rather than the internal movement characteristics in sloped channel. The present study applies two numerical models, namely, large eddy simulation (LES) and shallow water equations (SWEs) models embedded in the CFD software package FLOW-3D to analyze the internal movement characteristics of the dam-break flows and Favre waves, such as water level, the velocity distribution, the fluid particles acceleration and the bed shear stress, under the different bed slopes and water depth ratios. The results under the conditions considered in this study show that there is a flow state transition in the flow evolution for the steep bed slope even in water depth ratio α = 0.1 (α is the ratio of the tailwater depth to the reservoir water depth). The flow state transition shows that the wavefront changes from a breaking state to undular. Such flow transition is not observed for the horizontal slope and mild bed slope. The existence of the Favre waves leads to a significant increase of the vertical velocity and the vertical acceleration. In this situation, the SWEs model has poor

prediction. Analysis reveals that the variation of the maximum bed shear stress is affected by both the bed slope and tailwater depth. Under the same bed slope (e.g., S_0 = 0.02), the maximum bed shear stress position develops downstream of the dam when α = 0.1, while it develops towards the end of the reservoir when α = 0.7. For the same water depth ratio (e.g., α = 0.7), the maximum bed shear stress position always locates within the reservoir at S_0 = 0.02, while it appears in the downstream of the dam for S_0 = 0 and 0.003 after the flow evolves for a while. The comparison between the numerical simulation and experimental measurements shows that the LES model can predict the internal movement characteristics with satisfactory accuracy. This study improves the understanding of the effect of both the bed slope and the tailwater depth on the internal movement characteristics of the dam-break flows and Favre waves, which also provides a valuable reference for determining the flood embankment height and designing the channel bed anti-scouring facility.

Keywords: Dam-break flow; Bed slope; Wet bed; Velocity profile; Bed shear stress; Large eddy simulation.

1. Introduction

The evolution of the dam-break floods has attracted significant researchers and engineers' attention, primarily due to its huge destructive power to the human's lives and properties. It is necessary to implement corresponding flood emergency plans during the dam design and operation. In order to capture the propagation characteristic of the dam-break flows effectively and accurately, extensive studies have been carried out using various methods in the past decades (Stansby et al., 1998; Xia et al., 2010; Wang et al., 2016, 2018, 2020a). In addition, Favre waves will affect the navigation and transportation of ships and generate periodic pressure loads acting on the structures in the channel. In the design of the tailwater channel of hydropower station (such as the channel height

and the bottom erosion prevention) also need to consider the effect of Favre waves. The earliest systematic measurement was carried out by Favre (1935) in a rectangular flume. Subsequently, many researchers carried out further research on Favre waves (Peregrine, 1966; Treske, 1994; Marche et al., 1995; Soares-Frazao and Zech, 2002). Both dam-break flow and Favre waves can be generated by instantaneously lifting the gate in the channel. As for which kind of flow phenomenon will appear, it mainly depends on the relative relationship between the initially upstream and downstream water depths. According to the review made by Castro-Orgaz and Chanson (2020), dam-break flow will appear in the channel (the main feature is that the wavefront is broken) when the water depth ratio $\alpha < 0.4-0.55$ (α is the ratio of the tailwater depth to the reservoir water depth), and Favre waves will occur in the channel (the main feature is that the wavefront is undular) when the water depth ratio $\alpha > 0.4-0.55$. However, there are rarely studies on the internal movement characteristics of dam-break flows or Favre waves under the condition of sloping wet bed.

For the study of dam break waves, experimental studies mainly focus on the changes in water depth (Miller and Chaudhry, 1989; Lauber and Hager, 1998a, 1998b), propagation velocity (Leal et al., 2006; Marra et al., 2011) and pressure load (Chen et al., 2009) during the evolution of the dam-break flows. Considering different boundary conditions, Kocaman and Ozmen-Cagatay (2012) carried out laboratory experiment of the dam-break flows with laterally contracted cross-sections. In their experiments, the image processing technology was used to successfully capture the water depth change. They found that the water depth would increase in the contraction section, and the negative wave appeared after encountering the contraction section. The speed of the negative wave increased with the increase of the initial tailwater depth. Wang et al. (2019) used image processing technology to carry out laboratory experiments on both the rectangular and the triangular cross-sections, and

compared the evolution pattern and water depth change of the dam-break flows in the triangular and rectangular cross-sections. Liu et al. (2020) studied the propagation characteristics of the dam-break flows (water surface profile, wave height, wave speed, etc.) for different bed slopes and tailwater depths through the image processing technology. They found that the increase of the bed slope would accelerate the speed of shock wave and reduce the speed of the negative wave. The previous numerical simulation studies mainly focused on capturing the free surface (Savic and Holly, 1993; Chang et al., 2011; Marsooli and Wu, 2014), the sediment transport (Wu and Wang, 2007; Khosronejad et al., 2020a, 2020b), and the change of the turbulence intensity (Park et al., 2012). In the case of a horizontal bed, Shigematsu et al. (2004) studied the change of the water surface profile, and the distribution of velocity and turbulence intensity. They found that the location with large turbulence intensity mainly appeared within the bottom boundary area. Biscarini et al. (2010) compared the difference between the shallow water model and the full three-dimensional calculation through the numerical simulation of the dam-break flow. The analysis indicated that the shallow water model can obtain the main characteristics of the flow, but lose some three-dimensional information due to the simplification in the model. Khosronejad et al. (2019) used a coupled model to simulate the water surface and sediment transport in the dam break flow, and presented that the coupled model can accurately capture the scour processes of the river bed and the variation of the water surface. Taking the bed slope into account, Fraccarollo and Toro (1995) applied a shallow water model to analyze the water depth variation of the dam-break flow. They found that when there was a high free surface gradient in the dam-break flow, the calculated pressure and velocity distribution based on the shallow water model deviated greatly from the measurements.

For the research of Favre waves, Peregrine (1966) used numerical simulation to successfully

present the development process of Favre waves. The author pointed out that the maximum amplitude of the undulations is limited by breaking, and most of the measured breaking waves have the amplitude of about 0.6. Treske (1994) measured the water level elevations, the wave amplitude, the wave length and the frequencies of Favre waves in rectangular and trapezoidal open channels. He found that the primary wave undulations occur at Froude number ranging between 1.1 and 1.25, and the frequencies of secondary waves in the rectangular channel are about two to three times than that in the trapezoidal channel for the same Froude number. Soares-Frazao and Zech (2002) generated Favre waves in the flume by raising the gate instantaneously. After comparing the experimental results with their numerical calculation results, they found that the propagation of Favre waves is a typical weak non-hydrostatic flow, and the undulations appear if the Froude number ranges between 1 and 1.28. For higher Froude number, the wave front will break and lead to a steep front.

It can be seen that most of the above studies were carried out under the condition of either the horizontal bed or the slopping dry bed, and the focus of the previous studies were mainly on the macroscopic characteristics of the flow. However, the actual dam break flows or Favre waves are affected by both the bed slope and the tailwater (Wang et al., 2017, 2020b). The internal movement information (such as, velocity profile and bed shear stress distribution) is not only important for assessing the potential channel erosion damage (Shigematsu et al., 2004), but also a significant parameter for understanding and mitigating the impact of dam-break flood and Favre waves (Biscarini et al., 2010). Considering the limitation of the flume length (Liu et al., 2020) and the difficulty of collecting the internal flow characteristics, the purpose of this article is to better understand the internal characteristics of dam break flows and Favre waves under the conditions of the sloping wet bed by numerical simulation. The numerical model used in this article is

systematically validated by comparing with available experimental data (Barnes and Baldock, 2006; Larocque et al., 2013a; Liu et al., 2020). The dam-break flow and Favre waves under different bed slopes and tailwater depths are comprehensively analyzed in terms of water surface profile, velocity distribution, bed shear stress and fluid particles acceleration. The present study will further guide the preparation of flood control plans and the development of flood management, as well as the scheduling work in the channel and the design of the tailwater channel of hydropower station.

2. Numerical Models

The governing equations are discretized by the finite volume method in the commercial software FLOW-3D (Flow Science Inc., 2016), and many turbulence models are provided, such as prandtl mixing length model, standard k-ε model, k-ω model, large eddy simulation model and so on. The free water surface is captured using the Volume of Fluid (VOF) method that can accurately capture the changes of free water surface and has been widely used in the numerical simulation of dam-break flow in the past decades (Oertel and Bung, 2012; Kocaman and Ozmen-Cagatay, 2015; Yang et al., 2018a). In this paper FLOW-3D is applied to calculate the dam-break flow under different bed slopes and tailwater depths.

2.1. Navier-Stokes equations with large eddy simulation

In FLOW-3D, the continuity equation and momentum equations describing fluid motion have the following forms:

$$\frac{\partial(uA_x)}{\partial x}+\frac{\partial(vA_y)}{\partial y}+\frac{\partial(wA_z)}{\partial z}=0 \tag{1}$$

$$\frac{\partial u}{\partial t}+\frac{1}{V_F}(uA_x\frac{\partial u}{\partial x}+vA_y\frac{\partial u}{\partial y}+wA_z\frac{\partial u}{\partial z})=-\frac{1}{\rho}\frac{\partial p}{\partial x}+g_x+f_x \quad (2)$$

$$\frac{\partial v}{\partial t}+\frac{1}{V_F}(uA_x\frac{\partial v}{\partial x}+vA_y\frac{\partial v}{\partial y}+wA_z\frac{\partial v}{\partial z})=-\frac{1}{\rho}\frac{\partial p}{\partial y}+g_y+f_y \quad (3)$$

$$\frac{\partial w}{\partial t}+\frac{1}{V_F}(uA_x\frac{\partial w}{\partial x}+vA_y\frac{\partial w}{\partial y}+wA_z\frac{\partial w}{\partial z})=-\frac{1}{\rho}\frac{\partial p}{\partial z}+g_z+f_z \quad (4)$$

where u, v, w are the flow velocity in the three directions x, y, z, respectively, A_x, A_y, A_z are the fraction area open to flow at cell face in the three directions x, y, z, respectively (e.g., A_x is equal to the open area in the x direction divided by the cell edge area in the x direction), ρ is the fluid density, p is the pressure, V_F is the volume fraction (fraction of open volume in cell, it means that the cell is fully open when V_F equals to 1), g_x, g_y, g_z are the body acceleration in the three directions x, y, z, respectively, f_x, f_y, f_z are the viscous acceleration in the three directions of x, y, z, respectively.

To better simulate the turbulent flow, the computational grid is required to be sufficiently small to capture small vortex motion in the turbulent flow with reasonable computational cost. In this regard, the large eddy simulation (LES) approach is one of the options. Since the LES model can provide more details about the movement of the dam-break flow and has been widely used for the dam-break flow simulation (Bung, et al., 2008; Larocque et al., 2013a, 2013b; Khoshkonesh et al., 2019), it is applied in this study.

The LES model solves the turbulent motion that is larger than the grid scale directly through the Navier-Stokes equations, while the influence of the small-scale vortex is simulated by establishing a model, the so called sub-grid scale closure:

$$L=\left(\Delta x\Delta y\Delta z\right)^{1/3} \quad (5)$$

$$\tau_{ij}-\frac{1}{3}\tau_{kk}\delta_{ij}=-2\mu_t S_{ij}=-2(C_s L)^2\left|S_{ij}\right|S_{ij} \quad (6)$$

$$S_{ij} = \frac{1}{2}\left(\frac{\partial u_i}{\partial x_j} + \frac{\partial u_j}{\partial x_i}\right), \quad \left|S_{ij}\right| = \sqrt{2S_{ij}S_{ij}} \tag{7}$$

where L is the filter length, Δx, Δy, Δz are the grid sizes in the x, y, z directions respectively, the sub-grid scale tensor values are calculated using formulas (6) and (7), where μ_t, S_{ij}, and C_S are the turbulence viscosity, strain rate tensor and Smagorinsky's coefficient which is taken as 0.167 (Smagorinsky, 1963, Flow Science Inc., 2016, Khoshkonesh, 2019), respectively.

2.2. Shallow water equations model

For the comparison with the LES predictions, the shallow water equations (SWEs) model in FLOW-3D is also used in the study. The SWEs are obtained by performing water depth averaging processing on the three-dimensional incompressible Navier-Stokes equations. It can be used to describe the fluid flow when water depth is small comparing with the horizontal scales, and has a very broad application scenario (Soares-Frazao and Zech, 2002; Guo et al., 2012; Castro-Orgaz and Chanson, 2020). The SWEs model in FLOW-3D ignores the vertical acceleration of the flow and assumes that the movement of the flow satisfies the static pressure distribution. The continuity and momentum equations under 1D conditions read (Kocaman and Ozmen-Cagatay, 2015):

$$\frac{\partial(H - h_b)}{\partial t} + \frac{\partial\left[u(H - h_b)\right]}{\partial x} = 0 \tag{8}$$

$$\frac{\partial u}{\partial t} + u\frac{\partial u}{\partial x} = -\frac{1}{\rho}\frac{\partial p}{\partial x} + g_x + f_x \tag{9}$$

where u is water depth averaging velocity, h_b is the height of bottom contour and H is the surface elevation measured from the bottom of the grid. The SWEs model requires two layers of grids in the z direction, and the height of the bottom layer of grids needs to be greater than the maximum height that appears during the evolution of flow. The shallow water flow can reside in only one vertical

layer of control volumes (e.g., the bottom layer of cells in the *z* direction). The pressure in an element containing a free-surface is defined as follows:

$$p = p_0 + \rho g H \tag{10}$$

$$H = F V_F \delta_z + \left(1 - V_F\right) \delta_z \tag{11}$$

where p_0 is the atmospheric pressure on the free surface, δ_z is the cell size in the bottom layer, F is the fluid fraction, and V_F is the volume fraction (fraction of open volume in cell). The Sketch of related variables involved in the SWEs model in FLOW-3D is shown in the Figure 1. The volume/area blockages used in the FAVOR (Fractional Area/Volume Obstacle Representation) method can describe the geometry, and the water surface profile is tracked by the VOF method (Flow Science Inc., 2016).

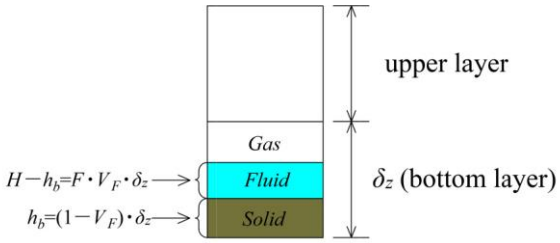

Fig. 1. Sketch of related variables involved in shallow water model

2.3. Initial and boundary conditions

The atmospheric pressure is specified at the free water surface. The outlet of the flume is set to outflow (Ozmen-Cagatay and Kocaman, 2012; Ozmen-Cagatay et al., 2014; Guo et al., 2014). No slip condition is applied to all solid boundaries, including the upstream end and bottom of the flume. Since no flux and shear of any property across the side wall, the side wall of the flume is set as symmetry. The water in the reservoir area and the downstream of the dam is initially at a static state, while the corresponding water depth is set according to the designed working conditions.

2.4. Numerical model setup

Taking into account the length limitation of the flume mentioned in the experiment of Liu et al. (2020), the reservoir area is extended to 18 m, and the downstream of the dam is extended to 19 m in the numerical simulation. In the numerical calculations, the upstream initial water depth h_u is 0.4 m. For the numerical simulation with the LES model, a solid gate is arranged at the dam position, and the movement of the gate is controlled by the General Moving Objects (GMO) module in FLOW-3D. The corresponding gate lifting speed is set to 2 m/s after comparing with the experimental conditions of Liu et al. (2020). The initial water in the reservoir area and downstream of the dam is imported through STereo Lithography (STL) files. The "history probe" in FLOW-3D is used to realize the function of marking particles. This kind of marking particles has no mass and will not affect the movement of the fluid. After setting it to follow the movement of the fluid, it is convenient to study the movement of a single fluid particle. As such, the internal motion characteristics of the dam-break flows can be studied in details through analyzing its trajectory and the acceleration variation of particles. The fluid particles with different position coordinates are set for analysis, and the corresponding position coordinates are shown in Table 1 (the position of the fluid particles is the same under the same water depth ratio for different bed slopes). The flume model in the numerical calculation is shown in Fig. 2, where h_u and h_d represent the initial upstream and downstream water depth respectively. The grid sizes in the x and z directions are 0.02m and 0.01m, respectively. Sensitivity analysis of the grid size in the y direction is mainly carried out in this study. The calculation results of different grid size are shown in Fig. 3 with h_u = 0.4 m and h_d = 0.04 m. It can be seen that the calculation results of the water surface profile and the velocity distribution have small difference. Considering the impact of calculation speed and accuracy, Δy = 0.02 m is used in

the subsequent numerical simulations. The final total number of grids are 4349850, 4812600, and 7681650 for S_0 = 0, 0.003 and 0.02, respectively. The time step is determined automatically in FLOW-3D, which is based on the Courant-Friedrichs-Lewy (CFL) criterion. In the SWEs model, the grid heights in the z direction are $\Delta z_1 = \Delta z_2 = 0.5$ m, $\Delta z_1 = \Delta z_2 = 0.7$ m, and $\Delta z_1 = \Delta z_2 = 1$ m for S_0 = 0, 0.003, and 0.02, respectively (where Δz_1 and Δz_2 are respectively the height of the bottom and top grids in the z direction), the horizontal grid Δx and the lateral grid Δy are 0.005 m in all simulation cases. The calculation grids for the three bed slope cases are all 14800, and calculation time is about 130 s for the dam-break flow evolution for 10 s. The computational grid system is shown in Table 2.

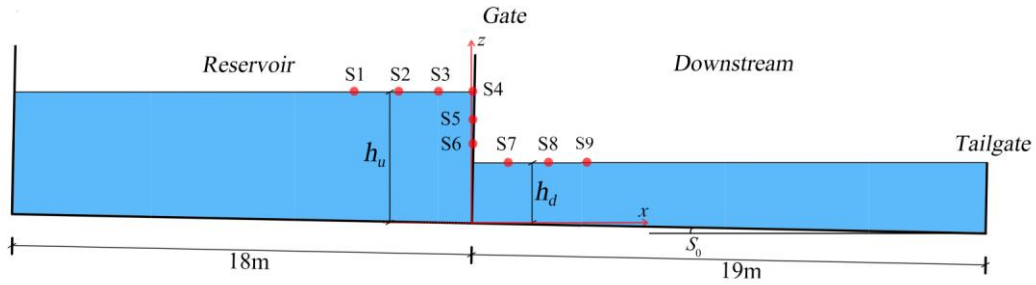

Fig. 2. Flume model in numerical simulation.

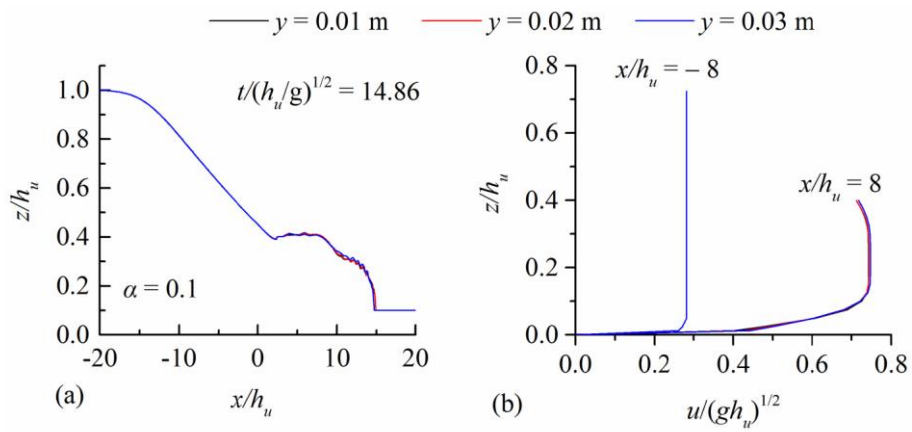

Fig. 3. Grid sensitivity analysis (a) water surface profile; (b) velocity profile.

Table 1. Mark particle coordinates.

α	S1		S2		S3		S4		S5		S6		S7		S8		S9	
	x/m	z/m	x/m	z/m	x/m	z/m	x/m	z/m	x/m	z/m	x/m	z/m	x/m	z/m	x/m	z/m	x/m	z/m
0.1	−3	0.40	−2	0.40	−1	0.40	0	0.40	0	0.30	0	0.20	1	0.04	2	0.04	3	0.04
0.3	−3	0.40	−2	0.40	−1	0.40	0	0.40	0	0.30	0	0.20	1	0.12	2	0.12	3	0.12
0.5	−3	0.40	−2	0.40	−1	0.40	0	0.40	0	0.33	0	0.26	1	0.20	2	0.20	3	0.20
0.7	−3	0.40	−2	0.40	−1	0.40	0	0.40	0	0.35	0	0.30	1	0.28	2	0.28	3	0.28

Table 2. Computational grid system for LES and SWEs models.

model	S_0	Δx (m)	Δy (m)	Δz (m)	number of real cells in $N_x \times N_y \times N_z$	total number of cells
LES	0	0.02	0.02	0.01	1851×50×47	4349850
LES	0.003	0.02	0.02	0.01	1851×50×52	4812600
LES	0.02	0.02	0.02	0.01	1851×50×83	7681650
SWE	0	0.005	0.005	0.5	7400×1×2	14800
SWE	0.003	0.005	0.005	0.7	7400×1×2	14800
SWE	0.02	0.005	0.005	1	7400×1×2	14800

3. Model validation

The accuracy of the numerical calculation results in terms of water surface profile, velocity distribution and bed shear stress are validated by comparing with previous experimental measurement results (the LES model is mainly calibrated here). In this section, we mainly focus on comparing the calculated velocity distribution and bed shear stress with the measurements of Larocque et al. (2013a) and Barnes and Baldock, (2006). The comparison with Liu et al., (2020) will be discussed in the section 4.1.

The first test case is an experimental conducted in the Hydraulics Laboratory, University of South Carolina in a smooth wooden flume (Larocque et al., 2013a). The experimental setup is shown in Fig. 4, the length of the reservoir area was 3.37 m, and the downstream length of the dam was 3.94 m. The flume was 0.18 m wide, 0.42 m high, and the bed slope was 0.93%. The water depth was

236 measured at different locations using a Baumer ultrasonic distance measuring sensor, and the
237 velocity was measured using UVP. The velocity distribution at different times for location 4 is used
238 for calibration under the experimental condition of h_u = 0.3 m and h_d = 0 m. The grid size used in the
239 first case is $\Delta x = \Delta y = \Delta z$ = 0.005 m with the total number of grids being 5368464, and the initial and
240 boundary conditions are set as section 2.3. The second test case was conducted at the University of
241 Queensland (UQ) Gordon McKay Hydraulics Laboratory with a dam break flume (Barnes and
242 Baldock, 2006). The main structure of the flume is shown in the Fig. 5. The length of the reservoir
243 was 2.25 m, and the downstream length of the dam was 1.75 m, the width of the flume was 0.4 m,
244 and the height was 0.4 m. The roughness height of the flume was about 0.1 mm. The bed shear stress
245 was measured using a novel shear plate at x = 0.45 m downstream of the dam for the dry horizontal
246 bed case. The water depth of the reservoir area was h_u = 0.2 m. The grid size used in the second case
247 is taken as $\Delta x = \Delta y = \Delta z$ = 0.005 m and the corresponding total number of grids is 4352000. The
248 initial and boundary conditions are also set as section 2.3. The relative root mean square error
249 (*RRMSE*) is used for estimating the difference between the results of the numerical simulation and
250 experimental measurements:

$$RRMSE = \sqrt{\frac{1}{n}\sum_{i=1}^{n}\left(\frac{s_i - e_i}{e_i}\right)^2} \tag{12}$$

251 where n is the total number of all measured data points, s_i is the numerical simulation value, e_i is
252 the measured value. The comparison result is shown in Fig. 6. It can be seen that the velocity
253 distribution of the numerical simulated agrees well with the experimental results. The velocity
254 distribution along the water depth all presents the typical characteristics of a bottom shear layer and
255 an upper stable layer. Analysis shows that the thickness of the shear layer roughly accounts for about
256 5% of the reservoir water depth, which is generally consistent with the result of Larocque et al.

257 (2013a). The calculated bed shear stress is also in good agreement with the experimental
258 measurements. In the case of h_u = 0.2 m, the maximum dimensionless bed shear stress is about 0.008
259 at x = 0.45 m. The results show that the LES model can be used to simulate the dam break flow with
260 satisfactory accuracy.

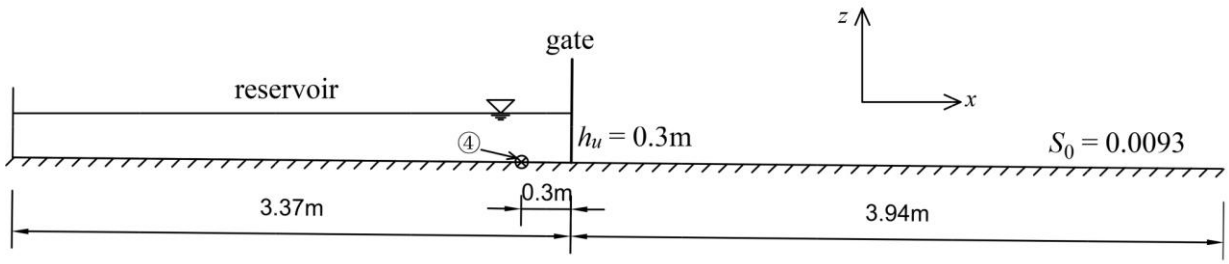

Fig. 4. Sketch of experimental set-up for validating the velocity profile.

261

262

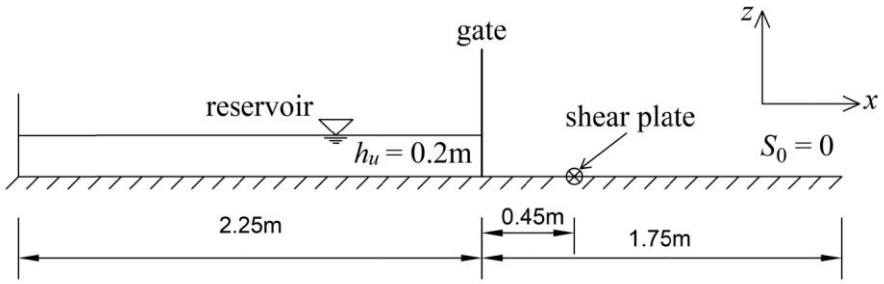

Fig. 5. Sketch of experimental set-up for validating the bed shear stress.

263

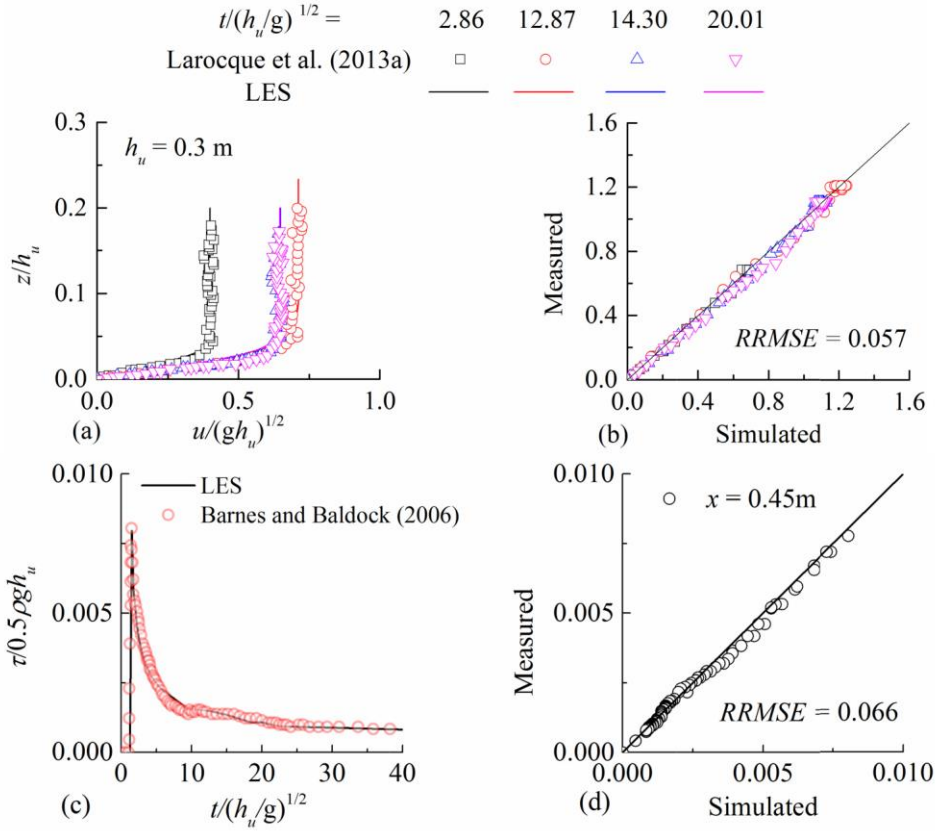

Fig. 6. Model validation results (a) variation of the velocity profile; (b) error value of the velocity profile; (c) variation of the bed shear stress; (d) error value of the bed shear stress.

4. Results

In order to facilitate the comparison and description of the propagation characteristics of the dam-break flow, the evolution area of the flow is generalized by different zones, as shown in Figure 7. In Figure 7, Zone 1 represents the area near the negative wavefront within the rarefaction wave, Zone 2 represents the area relatively far from the negative wavefront within the rarefaction wave, Zone 3 is the area affected by extra negative waves (Wang et al., 2020c, 2020d), Zone 4 is the shock wave area (its wavefront shape is marked with a dotted line, it mainly appears when the water depth ratio is relatively small (e.g., α = 0.1 and α = 0.3), and at this time the wavefront presents a steep front state), Zone 5 is an area where there is no obvious fluctuation near the dam (this area is not

affected by extra negative waves or Favre waves), and Zone 6 is the area affected by Favre waves (it mainly appears when the water depth ratio is relatively large, i.e. α = 0.5 and α = 0.7, at this time Favre waves appear in the wavefront).

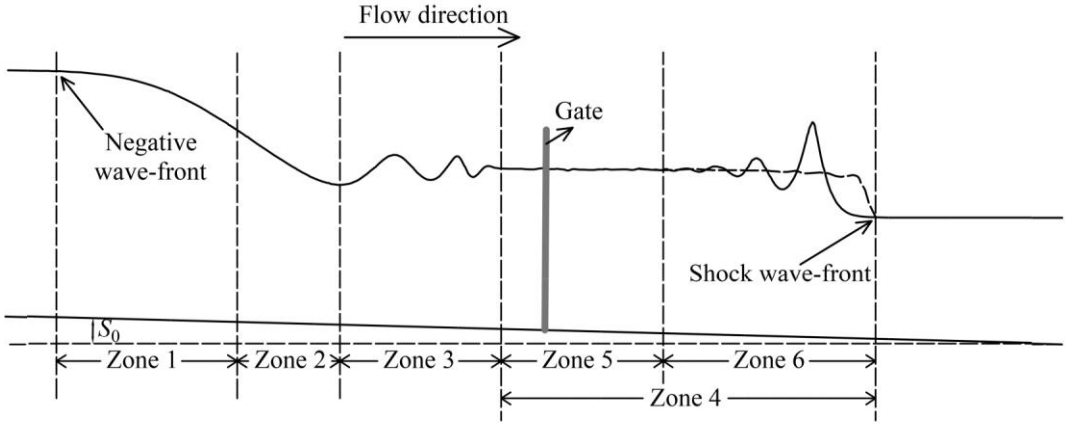

Fig. 7. Schematic diagram of regional division.

4.1. *Water surface profile*

The experimental results of Liu et al. (2020) are used to verify the accuracy of the numerical calculations in this section. The variation of water surface profile is shown in Figure 8. When α = 0.1, the LES results at $t/(h_u/g)^{1/2}$ = 4.95 − 19.81 are consistent with the experimental measurements. While, it is seen that the SWEs model is unable to capture the jumping phenomenon of the flow at the initial stage of the dam break (e.g., $t/(h_u/g)^{1/2}$ = 4.95) and the SWEs model prediction deviates from the experimental result in Zone 1. Favre waves do not appear throughout the entire evolution time for S_0 = 0, 0.003. However, for S_0 = 0.02, Favre waves gradually form in the late stage of the flow evolution (e.g., $t/(h_u/g)^{1/2}$ = 39.62). In addition, it is worth noting that its movement pattern changes during the evolution of the dam-break flows (the propagation form of wave front changes from steep bore to undular bore), and Favre waves cannot be captured by using the SWEs model. Mohapatra and Chaudhry (2004) found that when the water depth ratio is less than 0.4, the

calculation results of the SWEs model are basically consistent with the results of the Boussinesq-type models (nonhydrostatic pressure distribution models) in the case of horizontal bed. The present study found that when the bed slope is 0.02, even the water depth ratio is less than 0.4 (e.g., the water depth ratio is 0.1 or 0.3), there are fluctuations near the wavefront. The SWEs model underestimates the maximum water depth of the wavefront, while it can still capture of the wavefront position. Figure 9 shows the variation of Froude number for α = 0.1. When analyzing the propagation characteristics of Favre waves, *Fr* is calculated using the formula $Fr = (C_a - U_0)/C_0$ developed by Treske (1994), where C_a is the absolute speed of the wavefront, C_0 is the celerity defined as $C_0 = \sqrt{gh_0}$ (h_0 is water depth immediately in the wavefront), U_0 is the speed of the base flow downstream, equal to zero in this study. It can be found that when the bed slope $S_0 > 0$, *Fr* continues to decrease with the evolution of the flow. For the bed slope S_0 = 0.02, the *Fr* falls below 1.28 after $t/(h_u/g)^{1/2} > 31.5$ or $x_s/h_u > 36.9$. When the bed slope S_0 = 0.003, the *Fr* is much greater than 1.28 during the calculation period, so the Favre waves did not appear in this study. The variation of water depth in α = 0.3 is similar to that of α = 0.1, and the main difference is that Favre waves appear earlier when α = 0.3. The reason may be that the increase of the water depth ratio will cause a significant decrease in *Fr* (Liu et al., 2020). When α = 0.5 and 0.7, it is seen that the LES model can better capture the variation of the extra negative waves and Favre waves than the SWEs model. The results provided by the SWEs model differ greatly from the experiment in the Zone 3 and Zone 6, though the calculated water level in Zone 5 is in good agreement with the experiment. The flow state of the wavefront is still broken at S_0 = 0 in the late stage of the flow evolution (e.g., $t/(h_u/g)^{1/2}$ = 39.62), but it can better maintain the wave shape and continue to propagate steady downstream at S_0 = 0.003 for α = 0.5. This is consistent with the propagation state found by Liu et al., (2020). The flow

patterns basically show similar movement characteristics under the three different bed slopes, and Favre waves propagate downstream in a stable form for $\alpha = 0.7$.

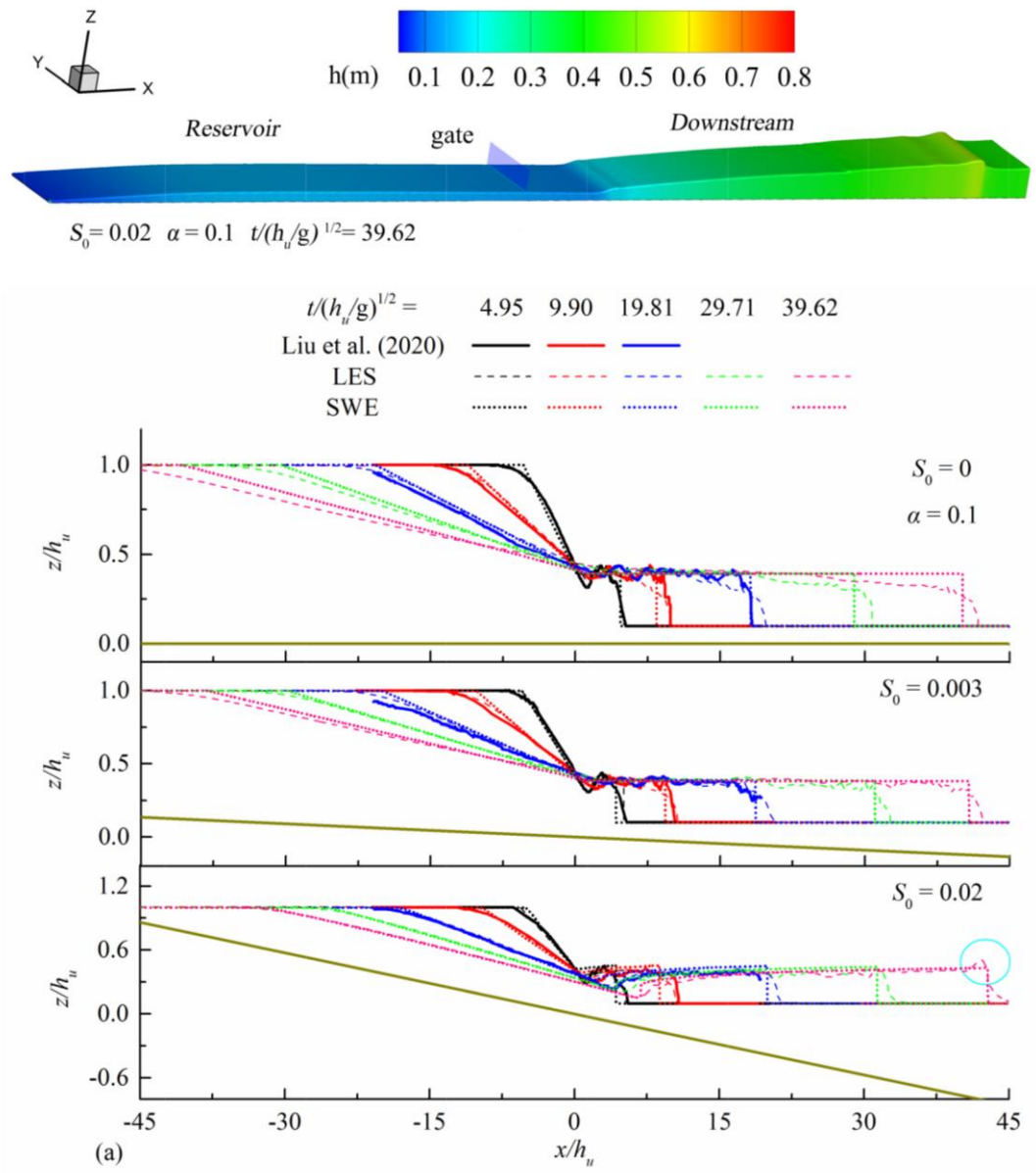

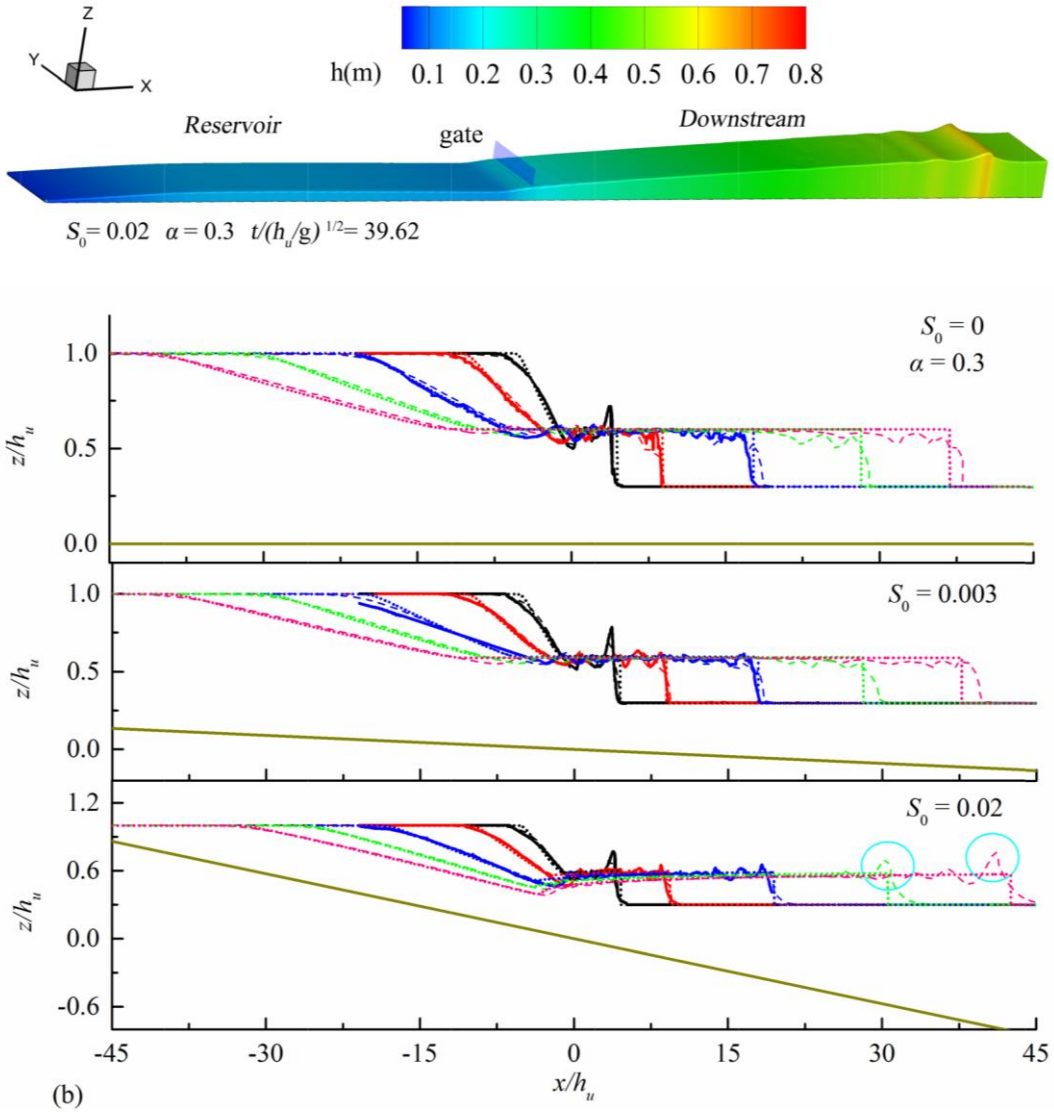
Z
Y
X
h(m) 0.1 0.2 0.3 0.4 0.5 0.6 0.7 0.8
Reservoir
gate
Downstream
S_0= 0.02 α = 0.3 $t/(h_u/g)^{1/2}$= 39.62
S_0 = 0
α = 0.3
S_0 = 0.003
S_0 = 0.02
z/h_u
x/h_u
1.0
0.5
0.0
1.2
0.6
-0.6
-45
-30
-15
0
15
30
45
(b)

318

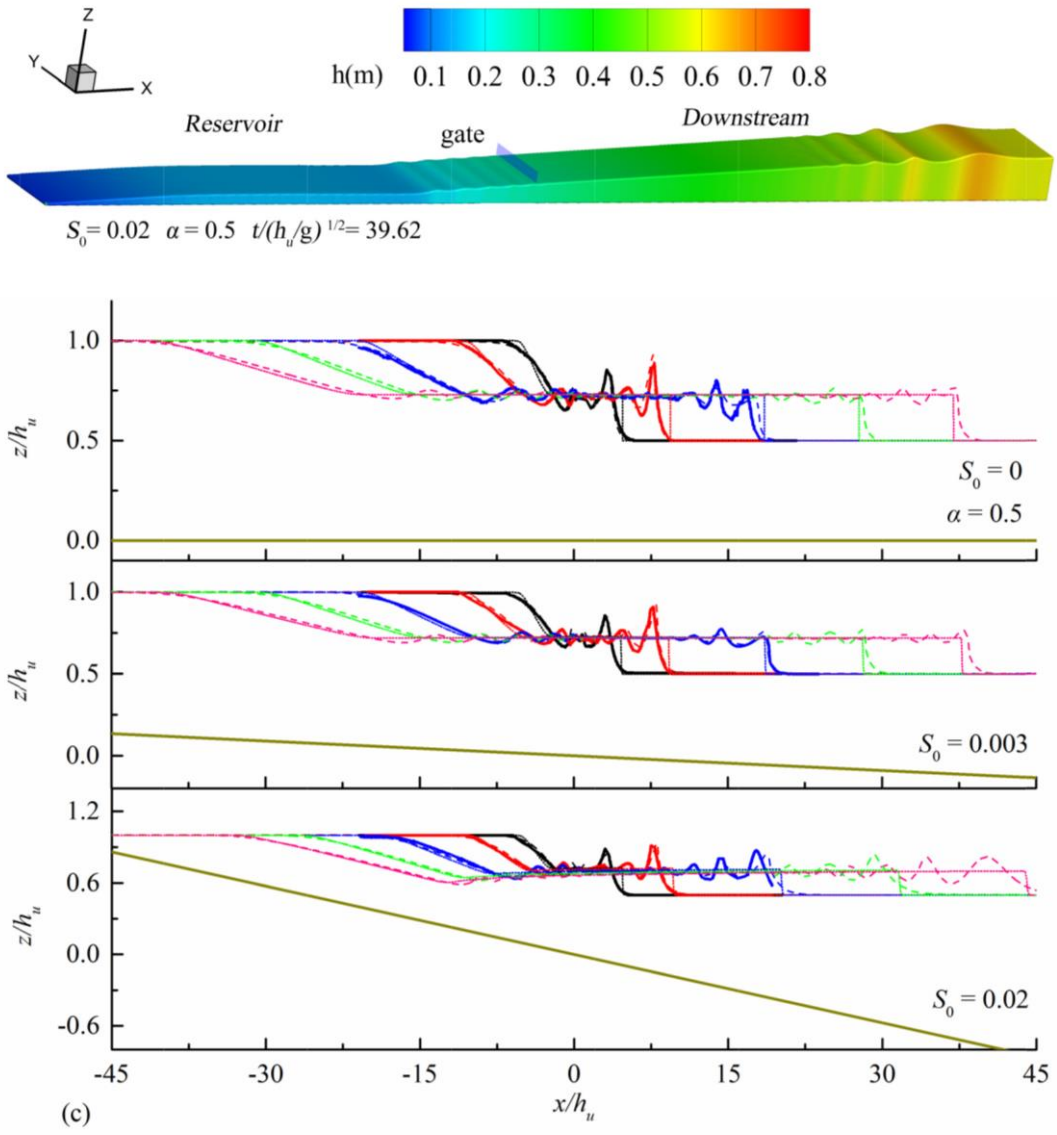
Z
Y
X
h(m) 0.1 0.2 0.3 0.4 0.5 0.6 0.7 0.8
Reservoir
gate
Downstream
S_0= 0.02 α = 0.5 $t/(h_u/g)^{1/2}$= 39.62
z/h_u
S_0 = 0
α = 0.5
S_0 = 0.003
S_0 = 0.02
x/h_u
(c)

319

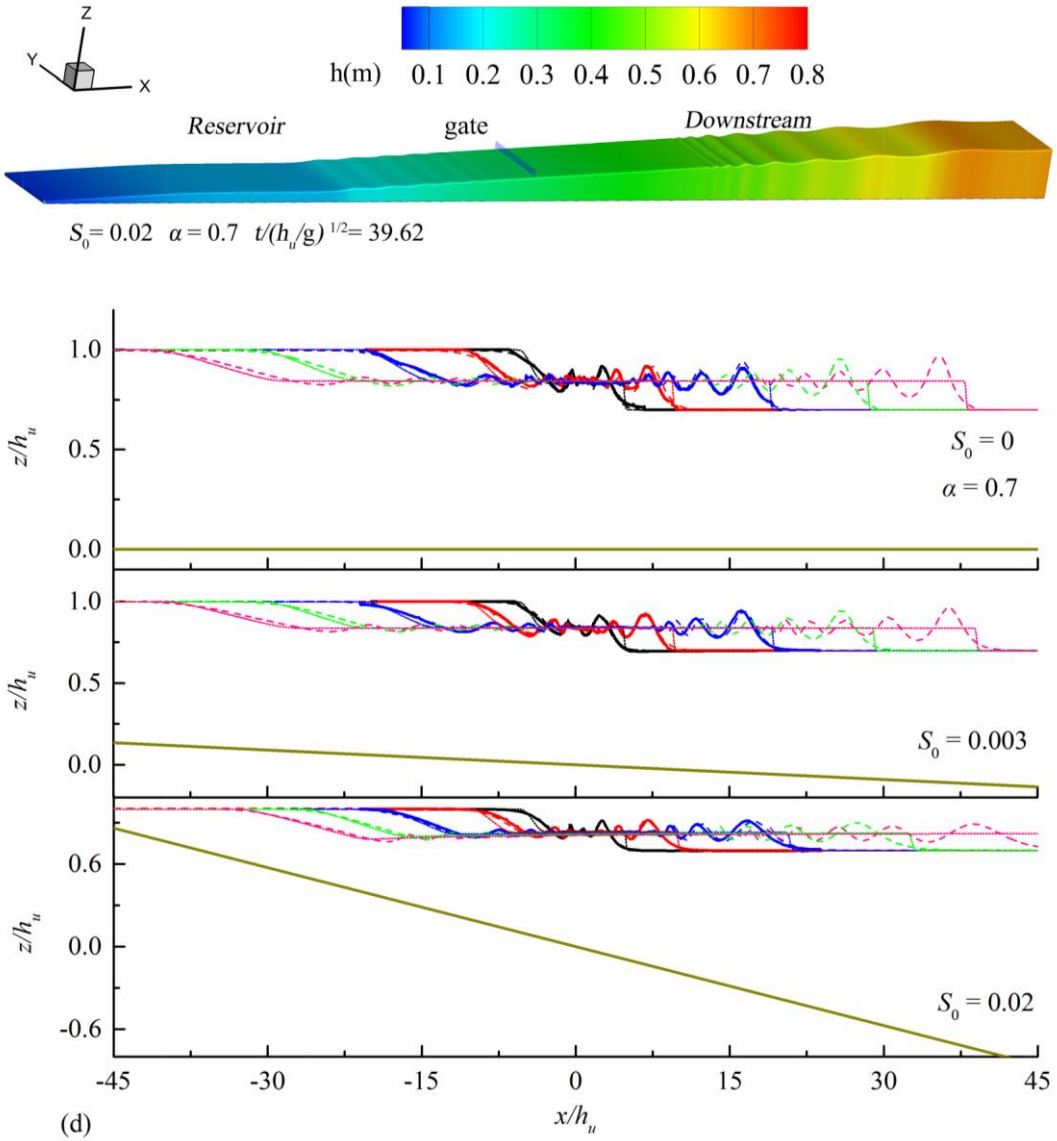

Fig. 8. Variation of water surface profile (a) α = 0.1; (b) α = 0.3; (c) α = 0.5; (d) α = 0.7.

320

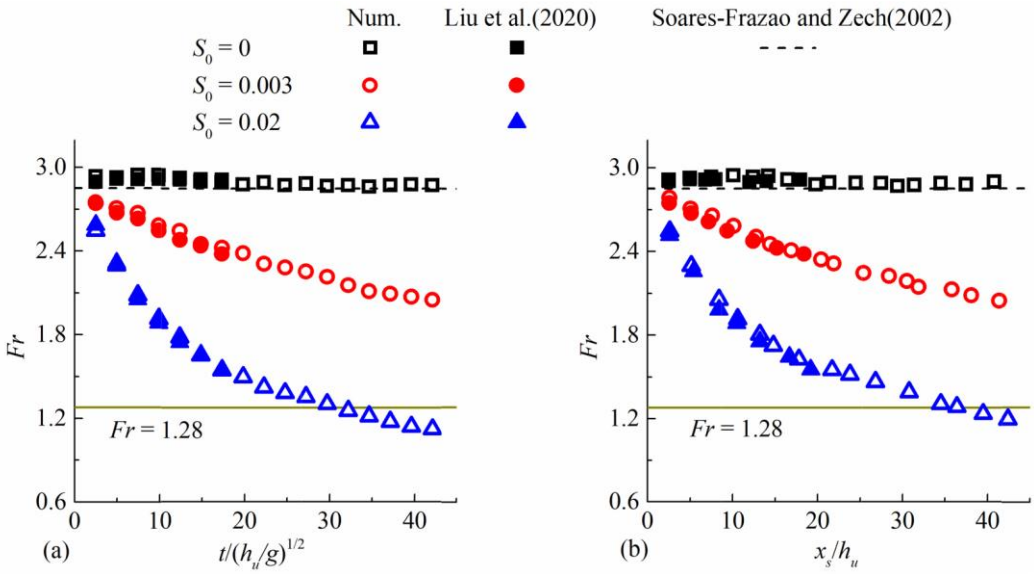

Fig. 9. Froude number for $\alpha = 0.1$ (a) variation with time; (b) variation with wavefront position.

321

322

323 **4.2. *Dimensionless velocity profile***

324 The cross-section positions for studying the velocity distribution under different bed slopes are
325 shown in Table 3 for $t/(h_u/g)^{1/2} = 14.86$. For the convenience of description, each position is marked
326 as P1 − P6 according to the coordinate value. Soares-Frazao and Zech (2002) found that ignoring the
327 vertical velocity may be a reason that the SWEs model could not accurately describe the Favre waves.
328 Yang et al. (2018b) also found that the results near the negative wave front produced from the SWEs
329 model greatly differed from the experimental measurements, and they found this difference was
330 mainly caused by the neglect of the vertical velocity. However, the previous analyses are all
331 qualitative descriptions, since there is no quantitative method for the proportion of the vertical
332 velocity in the past. This paper uses the following formulas (13 − 15) for the first time to quantify the
333 proportion of the vertical velocity:

$$\beta_h = \left| \frac{w}{u} \right| \tag{13}$$

$$\beta_p = \frac{\int_0^{h_s} \beta_h dh}{h_s} \times 100\% \tag{14}$$

$$\bar{\beta} = \frac{\int_{x_a}^{x_b} \beta_p dx}{x_b - x_a} \tag{15}$$

where β_h is the absolute value of the ratio of the vertical velocity over the horizontal velocity for a certain water depth at a fixed position, h_s is the local water depth at $t/(h_u/g)^{1/2}$ = 14.86, β_p is the depth-averaged proportion for a certain fixed position, x_a is the lower limit of the zone, x_b is the upper limit of the zone, and $\bar{\beta}$ is the average proportion of the vertical velocity within the zone. Table 4 lists the range of different zones. The distribution of the dimensionless horizontal velocity $U_x = u/(gh_u)^{1/2}$ (solid line) and the dimensionless vertical velocity $U_z = w/(gh_u)^{1/2}$ (scattered points) is shown in Fig. 10 and the proportion of the vertical velocity is shown in Fig. 11. When the velocity profile deviates either to the left or to the right, it means that the flow direction is opposite or the same as the positive direction of coordinate axis. When α = 0.1, the horizontal velocity of the reservoir area all presents the characteristic of the bottom shear layer and the upper stable layer, and the vertical velocity presents a linear increase from the bottom to the water surface, and the velocity profile all deviates to the left (the velocity direction is negative). The horizontal velocity at P6 presents the characteristic that the flow velocity of the upper water is obviously higher, especially in S_0 = 0.02. The reason may be that the upper water is firstly driven by the interaction between the wavefront and the downstream stationary water and the flow velocity increases in a short time, while the lower water needs longer time to gain energy via momentum and energy exchange. In the meantime, since the water depth at the downstream still water interacting with the wavefront increases with time at S_0 = 0.02, it takes longer for the velocity of the deep water to rise. When α = 0.3, the vertical velocity of P3 becomes positive, which is just the opposite of P4 under the effect of

353 the extra negative waves at $t/(h_u/g)^{1/2}$ = 14.86. The velocity distribution characteristic at α = 0.5 is
354 similar to that at α = 0.3 in general. It can be observed that the variation of the vertical velocity at P2,
355 P3 and P5, P6 are exactly the opposite for α = 0.7, indicating that the extra negative waves and Favre
356 waves have the opposite effects on the variation of the vertical velocity. The proportion of the
357 vertical velocity in Zone 1 is significantly larger than that in Zone 2 and 4 for α = 0.1. It may be the
358 reason that the result based on the SWEs model can't match very well near the negative wave front.
359 Although the water level at Zone 3 is affected by the extra negative waves at $t/(h_u/g)^{1/2}$ = 14.86, the
360 proportion of the vertical velocity in Zone 3 is still small for α = 0.3. It can be seen from the Fig. 11
361 that the influence of the extra negative waves on the vertical velocity becomes more important as the
362 water depth ratio increases. The proportion of the vertical velocity in Zone 3 increases at this time.
363 The Zone 5 has the smallest proportion of the vertical velocity comparing to other zone when α = 0.5
364 and 0.7. The proportion of the vertical velocity in Zone 6 (affected by Favre waves) shows a very
365 large value and gradually rises with the bed slope increases. It is obviously that the influence of the
366 vertical velocity cannot be ignored at this moment. From the above analysis, it can be concluded that
367 the distribution of the vertical velocity does not change uniformly along the water depth, and the
368 extra negative waves or Favre waves will increase the proportion of the vertical velocity. The
369 movement characteristics of the flow are also affected by the vertical velocity at this time. As such,
370 some assumptions in the shallow water model are no longer valid in this situation. Consequently, the
371 SWEs model is no longer applicable to describe the entire process of the dam-break flow evolution
372 (Marche et al., 1995; Soares-Frazao and Zech, 2002; Soares-Frazao and Guinot, 2008; Bristeau et al.,
373 2011; Cantero-Chinchilla et al., 2016).
374

Table 3. Dimensionless positions for studying the velocity distribution.

S_0	α	x/h_u (P1)	x/h_u (P2)	x/h_u (P3)	x/h_u (P4)	x/h_u (P5)	x/h_u (P6)
0	0.1	−12.5	−7.5	−2.5	0	7.5	12.5
0.003	0.1	−12.5	−7.5	−2.5	0	7.5	12.5
0.02	0.1	−12.5	−7.5	−2.5	0	7.5	13.8
0	0.3	−12.5	−7.5	−0.8	0.5	4.5	11.3
0.003	0.3	−10	−5	−0.8	0.6	7.5	12.5
0.02	0.3	−8.8	−5	−0.4	0.6	4.5	13.8
0	0.5	−10	−3.8	−2.1	0	3.5	12.5
0.003	0.5	−10	−3.8	−2.1	0	3.8	12.5
0.02	0.5	−8.8	−3.4	−1.9	3.8	12.5	14.3
0	0.7	−11.3	−6.3	−4.3	0	10.8	12.8
0.003	0.7	−11.3	−6.3	−4.3	2	11	13.3
0.02	0.7	−10	−5.8	−4.3	2	10.5	13

Table 4. Range of different zones for caclulating the average proportion of the vertical velocity.

S_0	α	x/h_u (Zone1)	x/h_u (Zone2)	x/h_u (Zone3)	x/h_u (Zone4)	x/h_u (Zone5)	x/h_u (Zone6)
0	0.1	[−19.5, −7]	[−7, 2]	−	[2, 15.1]	−	−
0.003	0.1	[−19, −7]	[−7, 2.7]	−	[2.7, 15.6]	−	−
0.02	0.1	[−17.5, −7]	[−7, 2.8]	−	[2.8, 16.6]	−	−
0	0.3	[−18, −7]	[−7, −2.1]	[−2.1, 3]	[3, 14.2]	−	−
0.003	0.3	[−17.5, −7]	[−7, −2]	[−2, 3]	[3, 14.9]	−	−
0.02	0.3	[−17, −7]	[−7, −1.4]	[−1.4, 3.2]	[3.2, 15.9]	−	−
0	0.5	[−18, −10]	[−10, −5.3]	[−5.3, 1]	−	[1, 5.4]	[5.4, 14.6]
0.003	0.5	[−17.5, −10]	[−10, −5]	[−5, 1.2]	−	[1.2, 5.5]	[5.5, 15.1]
0.02	0.5	[−16.5, −9]	[−9, −4.5]	[−4.5, 1.4]	−	[1.4, 5.8]	[5.8, 16.1]
0	0.7	[−17.5, −12]	[−12, −7.9]	[−7.9, 0]	−	[0, 4]	[4, 15.1]
0.003	0.7	[−17, −12]	[−12, −7.5]	[−7.5, −0.1]	−	[−0.1, 4.5]	[4.5, 15.4]
0.02	0.7	[−16, −11]	[−11, −7]	[−7, −0.5]	−	[−0.5, 4.6]	[4.6, 16.1]

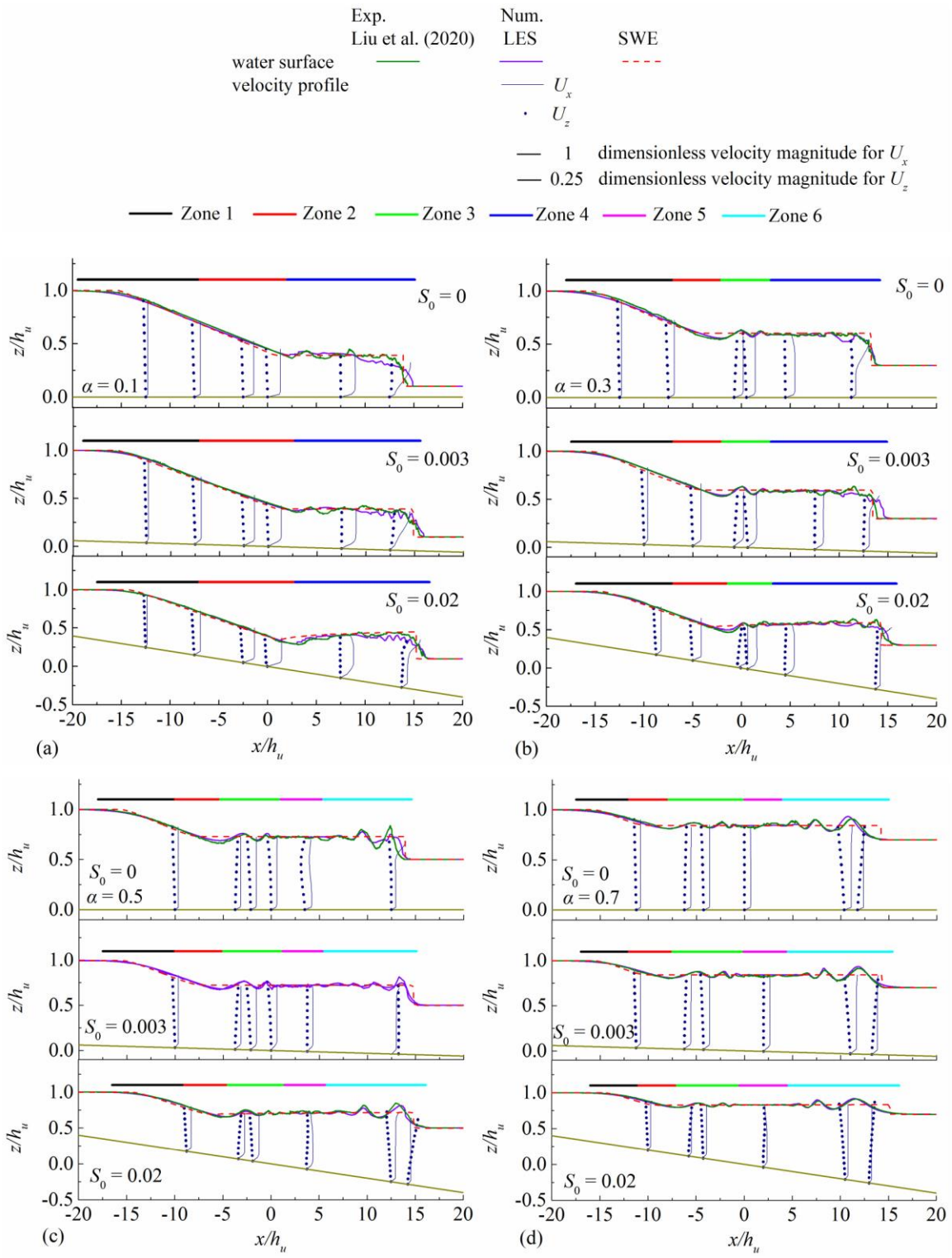

Fig. 10. Characteristics of velocity distribution at $t/(h_u/g)^{1/2} = 14.86$ (a) $\alpha = 0.1$; (b) $\alpha = 0.3$; (c) $\alpha = 0.5$; (d) $\alpha = 0.7$.

383

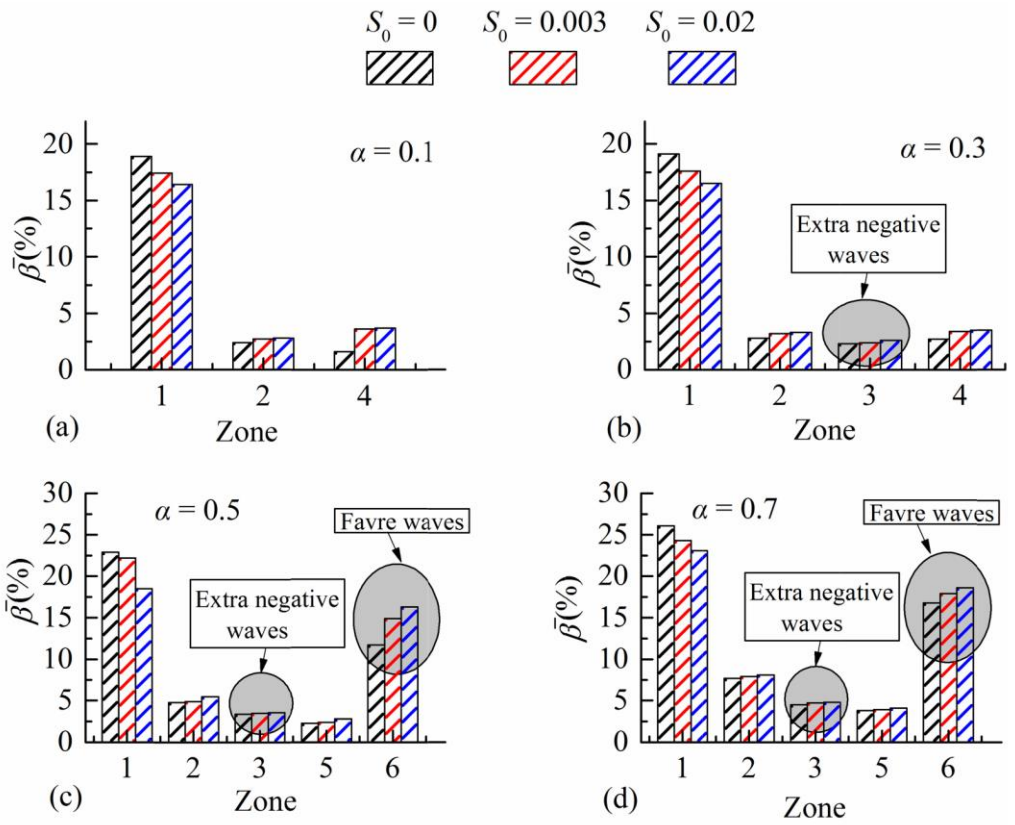

Fig. 11. Average proportion of the vertical velocity (a) $\alpha = 0.1$; (b) $\alpha = 0.3$; (c) $\alpha = 0.5$; (d) $\alpha = 0.7$.

4.3. *Bed shear stress distribution*

Figure 12 is the calculated bed shear stress distribution. When $\alpha = 0.1$, the LES results show that the bed shear stress in the wavefront has a high frequency oscillation phenomenon at $S_0 = 0$, 0.003. This is because the downstream water is relatively shallow at this moment and the interaction between the wavefront and the downstream stationary water is very intensive. However, the interaction is relatively weaker at $S_0 = 0.02$, and its high frequency oscillation effect no longer appears after $t/(h_u/g)^{1/2} > 4.95$. FLOW-3D uses a quadratic law to evaluate the bed shear stress in the SWEs model, and the formula is $\tau = \rho C_D u_d^2$ in the one-dimensional case. Where u_d is the depth-averaged velocity in the x direction, and C_d is a default value of 0.0026 in FLOW-3D, it is used to characterize the influence of frictional resistance. This value can simulate bed friction

relatively accurate in most cases according to the recommendation of FLOW-3D. In general, the SWEs model overestimates the bed shear stress. The depth-averaged velocity method does not seem to correctly predict the bed shear stress distribution. When α = 0.3，the LES results show that there is a fluctuation bed shear stress in the reservoir area (affected by the extra negative waves) and the bed shear stress at the wavefront also exhibits fluctuations due to the appearance of Favre waves at $t/(h_u/g)^{1/2}$ = 39.62 for S_0 = 0.02. The SWEs predictions are basically similar to those at α = 0.1. Obvious fluctuation appears in both the upstream and downstream reaches of the dam when α = 0.5 and 0.7 in the LES results, while the SWEs model cannot capture the fluctuation of the bed shear stress and underestimate the local bed shear stress in the fluctuating area. Therefore, when the water depth ratio is relatively high, in addition to considering the extra protection height of the embankment, it is also necessary to consider the increase in the bed shear stress caused by the waves, and take safer protection measures to prevent scouring. There are obvious differences in the variation of the bed shear stress under different bed slopes. Particularly, when the water depth is relatively large, the impact of the bed slope is more significant. The variation of the maximum bed shear stress position with time is shown in Fig. 13. When α = 0.1, it is seen that the maximum bed shear stress always occurs near the dam site. The variation of the maximum bed shear stress position with time is almost the same when $t/(h_u/g)^{1/2} \leq 15$ for three bed slopes. However, the position moves farther with the increase of the bed slope after $t/(h_u/g)^{1/2} > 15$. The maximum bed shear stress position appears downstream of the dam when $t/(h_u/g)^{1/2} \leq 3.96$ and moves into the reservoir area after $t/(h_u/g)^{1/2} > 3.96$ for α = 0.3. After the gate is lifted, the water in the reservoir area subducts downstream of the dam at a very fast speed in the early stage, resulting in a relatively large bed shear stress in the downstream of the dam. And then, due to the adjustment of the flow velocity, the maximum bed

418 shear stress gradually developed towards the end of the reservoir. When α = 0.5, it can be found that
419 the maximum bed shear stress firstly appears downstream near the dam, and moves towards the
420 reservoir area, and it moves downstream of the dam again when $t/(h_u/g)^{1/2} \geq 35.66$. It can be found
421 from Figure 12(c) that the maximum bed shear stress in the reservoir area is significantly greater than
422 that in the downstream of the dam in the early stage of the dam-break flow, however, because the
423 maximum bed shear stress in the reservoir area continues to decrease over time, the maximum bed
424 shear stress in the downstream of the dam will exceed that in the reservoir area in the latter stage.
425 However, for sloping bed (i.e. S_0 = 0.003 and 0.02), the maximum bed shear stress always appears in
426 the reservoir area. For the case of S_0 = 0.003, as the water depth in the reservoir area is slightly
427 reduced compared to the horizontal bed, the maximum bed shear stress in the reservoir area
428 decreases slowly compared to the horizontal bed. Simultaneously, the bed shear stress in the
429 downstream of the dam is reduced due to the increase in the water depth downstream of the dam.
430 Therefore, during the entire simulation period, the location of the maximum bed shear stress is in the
431 reservoir area. As for S_0 = 0.02, the effect of water depth changes is more significant. The maximum
432 bed shear stress in the reservoir area has the characteristic of increasing over time, while the bed
433 shear stress downstream of the dam has dropped significantly. In the case of α = 0.7, the maximum
434 bed shear stress occurs in the reservoir area when $t/(h_u/g)^{1/2} \leq 5.94$ and then develops towards
435 downstream of the dam for S_0 = 0, and 0.003, while it continues to develop towards the end of the
436 reservoir for S_0 = 0.02. For the condition of S_0 = 0 and 0.003, the appearance of Favre waves
437 increases the bed shear stress downstream of the dam, but at S_0 = 0.02, the increase in the
438 downstream water depth leads to a more significant decrease in the shear velocity, at this time the
439 bed shear stress still shows a downward trend. Figure 14 plots the time when the maximum bed shear

stress appears at different positions. When α = 0.1, the bed shear stress has been rising during the simulated time period ($t/(h_u/g)^{1/2}$ = 39.62) at the reservoir position $x/h_u \leq -12.5$ for S_0 = 0 and 0.003, so the time when the maximum bed shear stress appears at these locations is not shown here. But when $-12.5 < x/h_u < 0$, it can be seen that the time when the maximum bed shear stress appears earlier at S_0 = 0 than that at S_0 = 0.003 for the same dimensionless position. It can be seen from Figure 14(c) and 14(d) that the large reduction of water depth in the reservoir area enables the shear velocity to be maintained at a higher level for a long duration when S_0 = 0.02. Correspondingly, the time when the maximum bed shear stress appears in the reservoir area is delayed. As for the situation downstream of the dam, the time when the maximum bed shear stress appears is later at S_0 = 0.02 than that at S_0 = 0 and 0.003 for the same dimensionless position when $0 < x/h_u < 17.5$, while the situation is the opposite when $x/h_u \geq 17.5$. When α = 0.3, the time when the maximum bed shear stress appears at the reservoir location $x/h_u = -12.5$ is earlier than that at α = 0.1. It can be found that the furthest location of the reservoir area where the maximum bed shear stress can occur within the simulation time range is continuously developing toward the end of the reservoir as the water depth ratio increases. The time when the maximum bed shear stress appears is later for larger bed slope at the same dimensionless position, but for the situation of the downstream of dam, the conclusion is the opposite for α = 0.5 and 0.7.

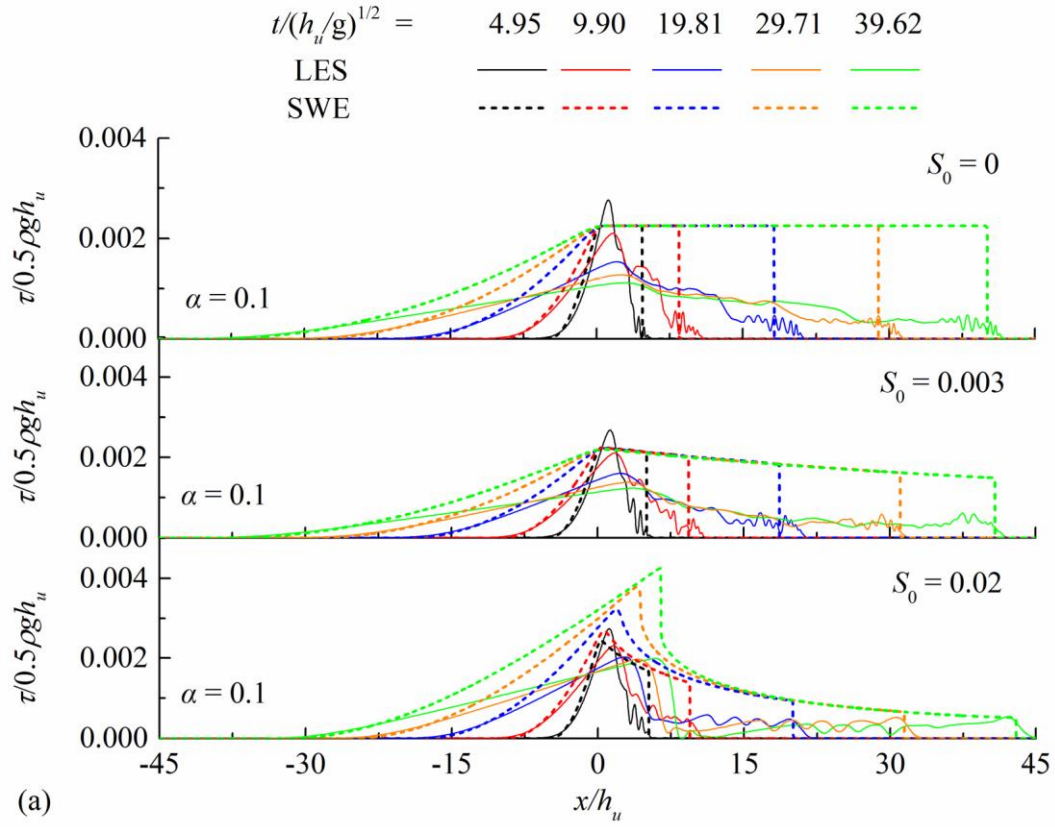
$t/(h_u/g)^{1/2}$ = 4.95 9.90 19.81 29.71 39.62
LES
SWE
$S_0 = 0$
$S_0 = 0.003$
$S_0 = 0.02$
$\alpha = 0.1$
$\tau/0.5\rho g h_u$
0.004
0.002
0.000
-45 -30 -15 0 15 30 45
x/h_u

(a)

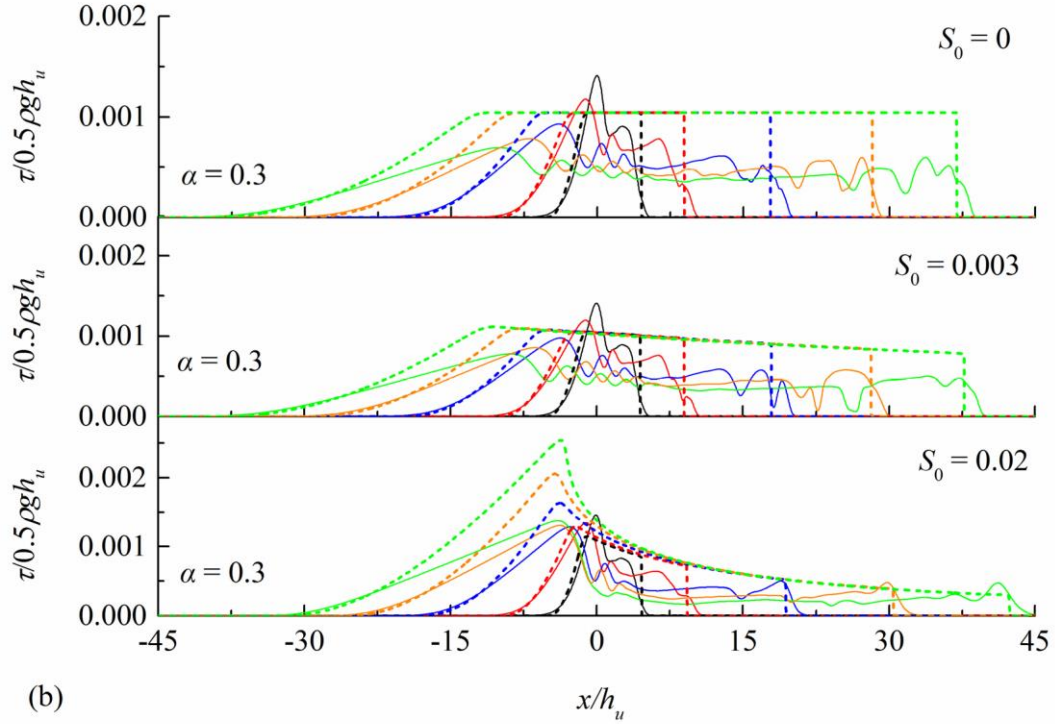
$S_0 = 0$
$S_0 = 0.003$
$S_0 = 0.02$
$\alpha = 0.3$
$\tau/0.5\rho g h_u$
0.002
0.001
0.000
-45 -30 -15 0 15 30 45
x/h_u

(b)

457

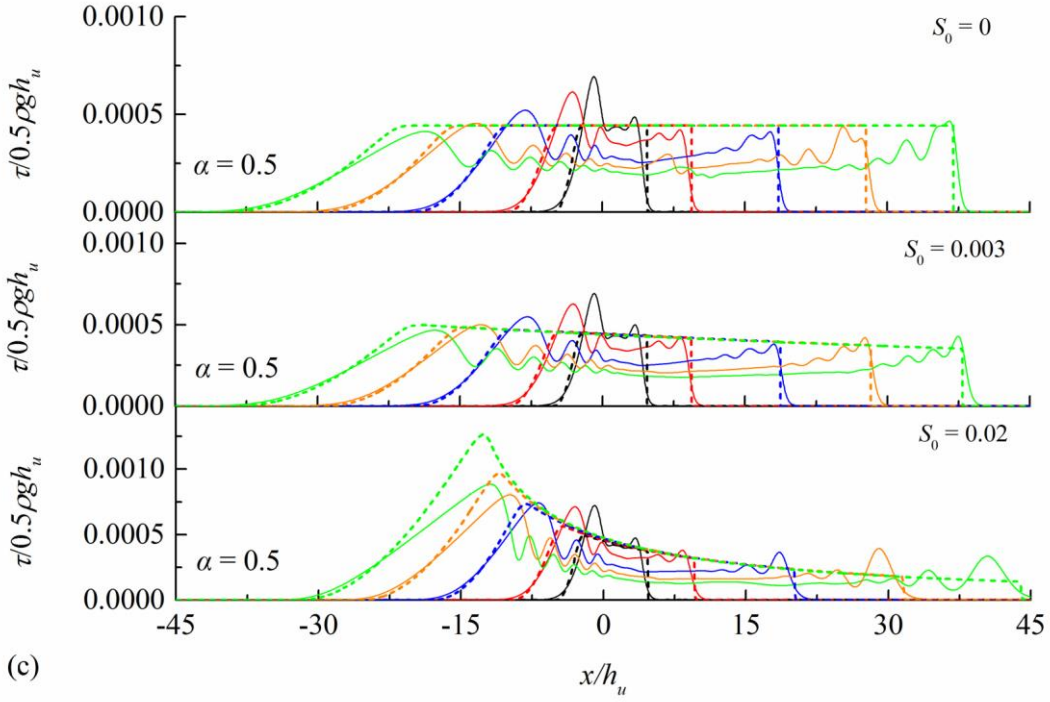

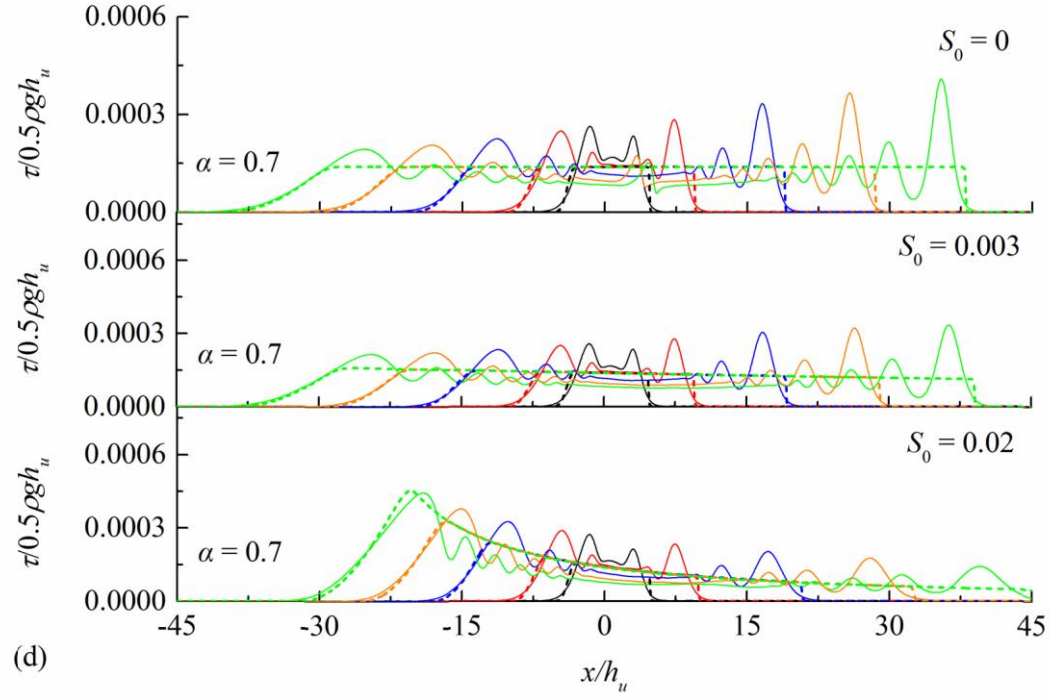

Fig. 12. Bed shear stress distribution (a) $\alpha = 0.1$; (b) $\alpha = 0.3$; (c) $\alpha = 0.5$; (d) $\alpha = 0.7$.

458

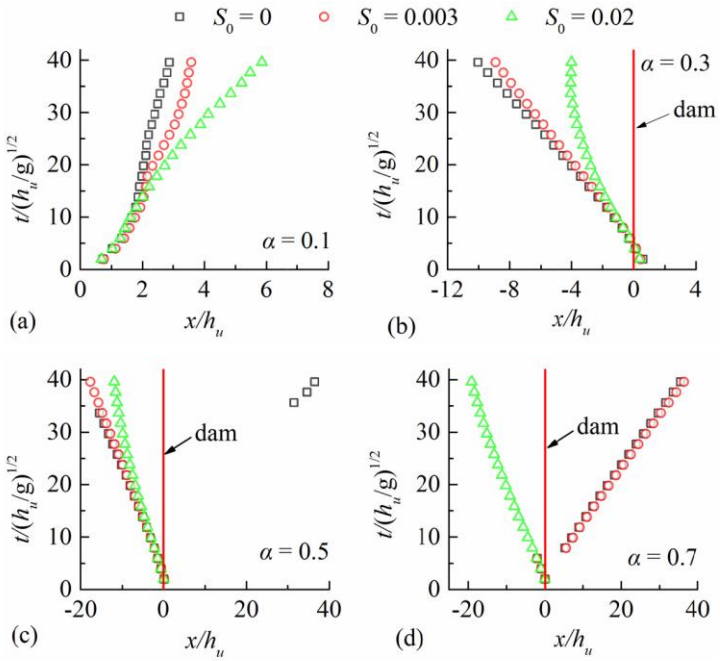

Fig. 13. Variation of the maximum bed shear stress position with time (a) $\alpha = 0.1$; (b) $\alpha = 0.3$; (c) $\alpha = 0.5$; (d) $\alpha = 0.7$.

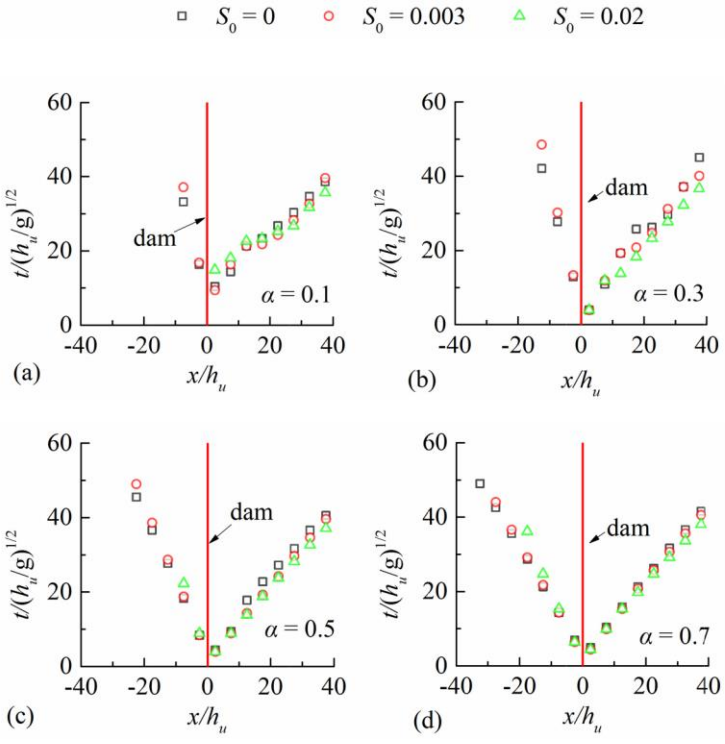

Fig. 14. Time when the maximum bed shear stress appears at different positions (a) $\alpha = 0.1$; (b) $\alpha = 0.3$; (c) $\alpha = 0.5$; (d) $\alpha = 0.7$.

4.4. *Fluid particles movement trajectory and acceleration variation*

The analysis of the fluid particles movement trajectory can provide a deeper understanding of the internal characteristics of the flow. The analysis of particles acceleration can provide a reference for the application of related simplified mathematical models (such as the SWEs model). Figure 15 shows the movement characteristics of the fluid particles for different water depth ratios, among them, the top image represents the motion trajectory of the particles, and the middle and bottom images are the dimensionless horizontal and vertical acceleration of the particles respectively, and $B_x = b_x/g$, $B_z = b_z/g$, where b_x and b_z are horizontal and vertical acceleration of fluid particle respectively. It is found that the movement characteristics (e.g. acceleration changes) of the particles (S1, S2 and S3) in the reservoir area are basically the same, so are the particles in the dam location (particles S4, S5 and S6) and downstream of the dam (particles S7, S8 and S9). For convenience, only the movement of S2, S5, S8 is selected for analysis. When $\alpha = 0.1$, the water level of the particle S2 in the reservoir area gradually recovers to stable state after falling for a period of time, and its horizontal and vertical acceleration are very small. The water level of the particle S5 at the dam location decreases sharply in a very short time, and the horizontal and vertical accelerations at the initial stage are relatively large, but only maintain for a very short time. Both the horizontal and the vertical accelerations decrease and approach to 0 after $t/(h_u/g)^{1/2} \geq 4.95$. The acceleration change of the particle S8 also has a similar feature to S5. When $\alpha = 0.3$, the water level of the particle S2 in the reservoir area has a minor fluctuations after $t/(h_u/g)^{1/2} \geq 9.90$, which is affected by the extra negative waves, and the horizontal and the vertical accelerations are still small. The horizontal and the vertical acceleration of the particle S5 at the dam location is similar to that when $\alpha = 0.1$. The water level of the particle S8 gradually stabilizes after rising slowly. The acceleration variation characteristics is

almost the same as that at α = 0.1. When α = 0.5, the water level of the particle S2 in the reservoir area appears a small fluctuations after a period of decline, and the horizontal and the vertical accelerations also show weak fluctuations at this time. The water level of the particle S5 at the dam location fluctuates after a rapid decline at S_0 = 0 and 0.003, while the water level continues to decrease in the later stage of the dam-break flows at S_0 = 0.02 (e.g., $t/(h_u/g)^{1/2} \geq 9.90$). The acceleration change of particle S5 is very similar under the three bed slopes with all having a big acceleration at the early short stage and reduces to near 0 in the later stage. The water level of the particle S8 forms a steep peak when the dam-break flow spreads to this location, and it then gradually decreases and fluctuates again in the later stage ($t/(h_u/g)^{1/2} \geq 29.71$). The horizontal and the vertical accelerations are maintained at large value when $t/(h_u/g)^{1/2} \leq 9.90$, and it appears a weak fluctuation in the later stage. When α = 0.7, the movement characteristic of the particle S2 and S5 is very similar to that at α = 0.5. The main difference is the movement of particle S8. Its water level affected by Favre waves appears fluctuation, and it gradually returns to stability after $t/(h_u/g)^{1/2} \geq$ 19.81. The horizontal and the vertical accelerations also fluctuate when Favre waves are formed, and the magnitude of the vertical acceleration is roughly equal to the horizontal acceleration, which means that the vertical acceleration can't be neglected in this moment. This may be a reason that the SWEs model cannot accurately capture the free-surface undulations in the wavefront.

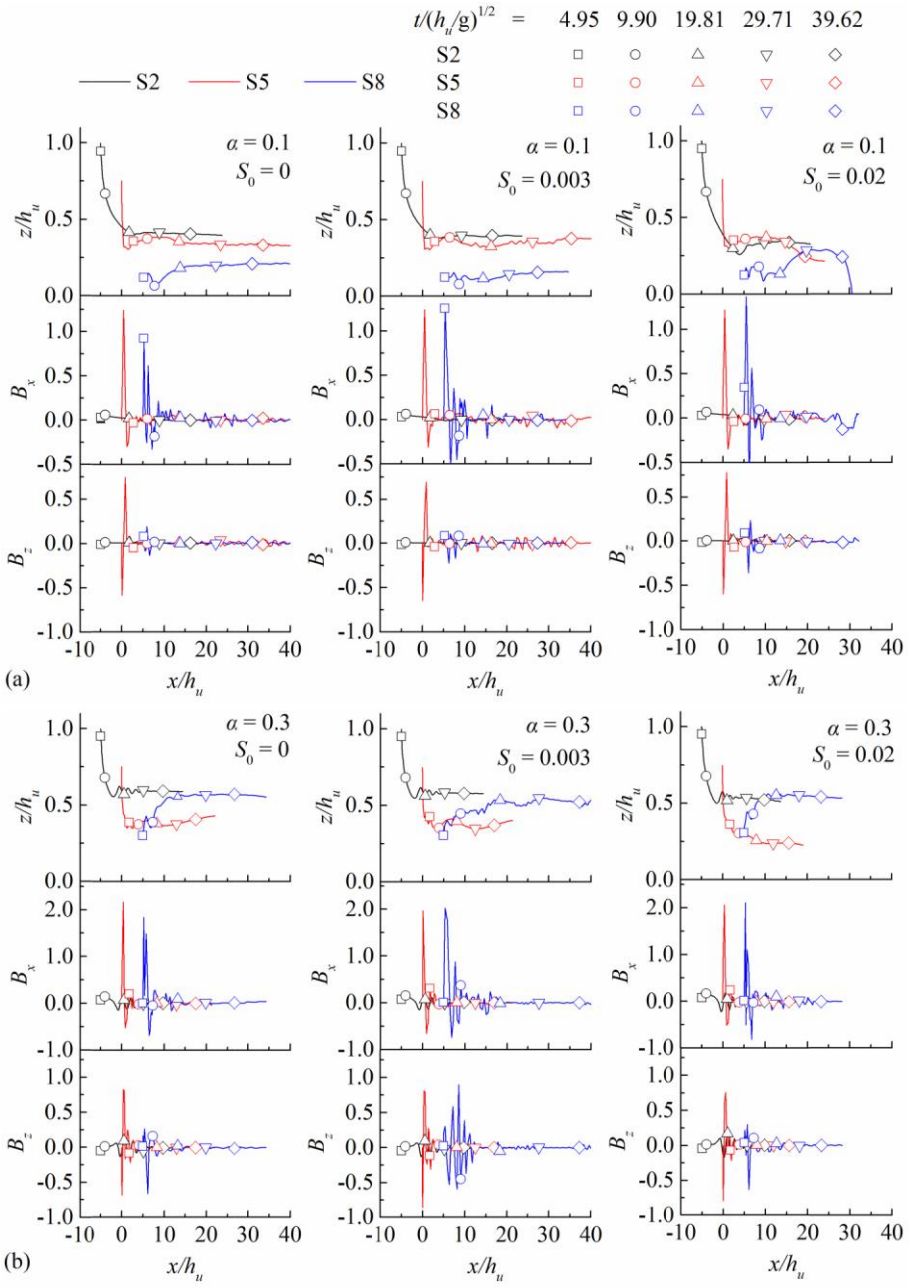
$t/(h_u/g)^{1/2}$ = 4.95 9.90 19.81 29.71 39.62
S2
S5
S8
$\alpha = 0.1$
$S_0 = 0$
$\alpha = 0.1$
$S_0 = 0.003$
$\alpha = 0.1$
$S_0 = 0.02$
$\alpha = 0.3$
$S_0 = 0$
$\alpha = 0.3$
$S_0 = 0.003$
$\alpha = 0.3$
$S_0 = 0.02$
z/h_u
B_x
B_z
x/h_u
(a)
(b)

502

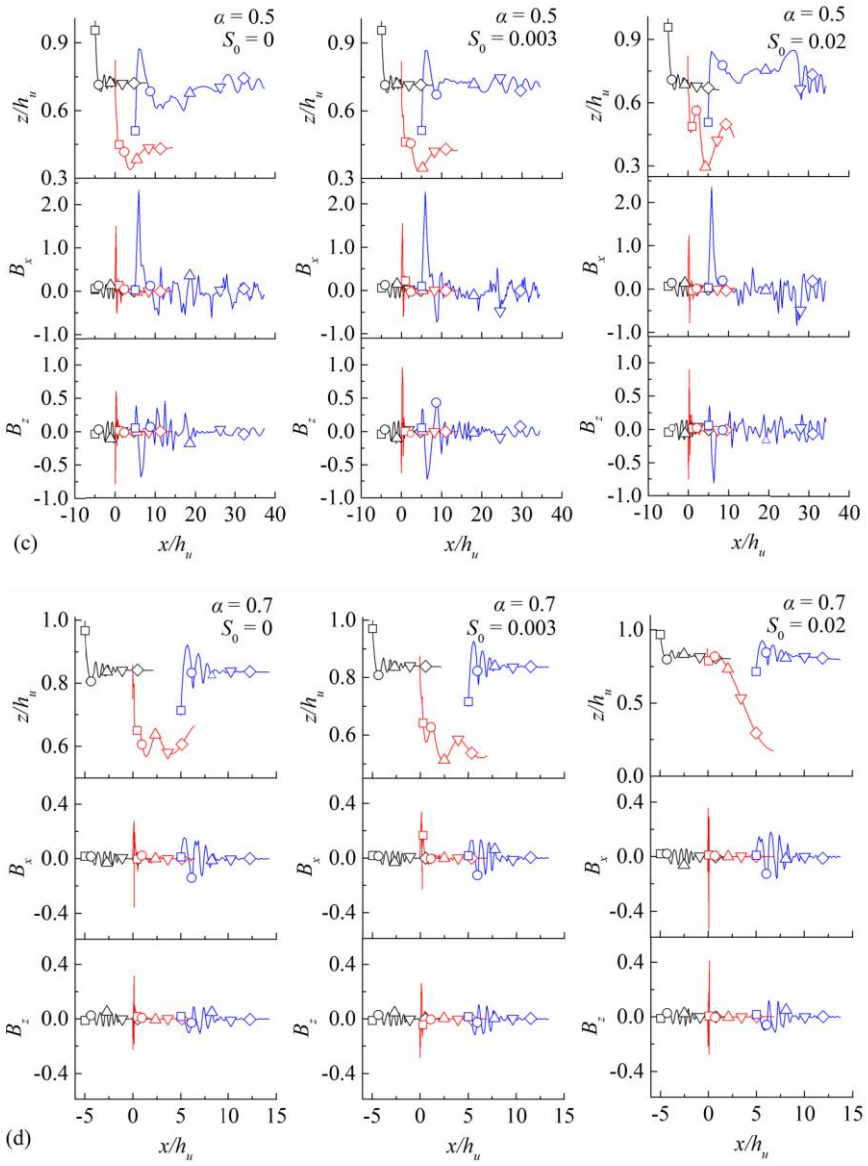

Fig. 15. Movement characteristics of the fluid particles (a) $\alpha = 0.1$; (b) $\alpha = 0.3$; (c) $\alpha = 0.5$; (d) $\alpha = 0.7$.

5. Conclusions

In this study, FLOW-3D is applied to conduct detailed numerical simulation on the dam-break flow under different bed slopes and water depth ratios. The internal movement characteristics have been analyzed. The main conclusions are as follows:

1. For the dam break flow propagating along the steep wet bed (e.g. $S_0 = 0.02$), the downstream static water depth that interacts with the wave front increases significantly, so that the *Fr* decreases with the evolution of the dam-break flow (Liu et al., 2020). Even under the condition of

512 the initial water depth ratio of 0.1, the phenomenon of Favre waves will appear after a relatively long
513 evolution time. However, this phenomenon does not appear for the horizontal and the mild bed slope
514 (i.e. S_0 = 0 and 0.003) in the present tests.

515 2. The vertical velocity and vertical acceleration increase under the influence of Favre waves.
516 It is found that the vertical velocity can reach about 26.1% of the horizontal velocity, while the
517 maximum vertical acceleration is approximately 74.1% of the maximum horizontal acceleration
518 when α = 0.7. This means that the vertical movement plays an important role in this moment. This
519 may be one of the reasons that the SWEs model cannot accurately describe this fluctuation
520 phenomenon.

521 3. The bed slope and the water depth have a coupling relationship in both the upstream and the
522 downstream reservoir in current cases. It is found that the water depth has a significant impact on the
523 variation of the bed shear stress. When α = 0.7, the peak value of the bed shear stress in the reservoir
524 area continues to rise with the evolution of the dam-break flow at S_0 = 0.02, while it continues to
525 decline for the horizontal and the mild bed slope (i.e. S_0 = 0 and 0.003). For the downstream of dam,
526 the situation is opposite.

527 Although the shallow water equations models failed to capture some detail of the flow
528 movement, the average results are generally acceptable. Considering that the 3D calculation requires
529 more calculation costs, it is feasible to use the calculation results of the shallow water equations
530 models to guide the work when the water depth ratio and the bed slope are small. But when the water
531 depth ratio or the bed slope is larger (especially when Favre waves appear in the channel), the
532 calculation of the shallow water equations models will ignore the influence of Favre waves. This
533 study shows that flow state is significantly affected by the bed slope, especially when the bed slope is
534 large (e.g., S_0 = 0.02). Favre waves are formed at the later stage even in the small water depth ratio
535 (e.g., α = 0.1). Generally, the actual bed slope is not so large, but the occurrence of this phenomenon
536 has an obvious temporal cumulative effect, Favre waves will also appear as long as the evolution

time is long enough even when the bed slope is small. Considering that Favre waves will obviously increase the wavefront height and causes the difficulty of flood control, the influence of the bed slope should be taken into account when selecting the height of the flood embankment. In addition, it is often necessary to use gates to adjust flow discharge in the canals. Because the maximum bed shear stress presents different characteristics under different bed slopes and tailwater depths, it is necessary to take into account the influence of the bed slope and the water depth ratio at the same time for better formulating the riverbed anti-scouring plans.

Declaration of Competing Interest

The authors declare that they have no conflict of interest.

Acknowledgements

This study is supported by the National Natural Science Foundation of China (Grant No: 51879179, 52079081), the Open Fund from the State Key Laboratory of Hydraulics and Mountain River Engineering, Sichuan University (SKHL1809) and the Sichuan Science and Technology Program (No. 2019JDTD0007). We thank the Associate Editor and two anonymous reviewers for their constructive comments for improving the quality of this final paper.

Notation

The following symbols are used in this paper:

A = fraction area;

b = acceleration of fluid particle movement;

B = dimensionless acceleration of fluid particle movement;

C_S = Smagorinsky's coefficient;

f = viscous acceleration;

562 Fr = Froude number;

563 g = body acceleration;

564 h = water depth;

565 H = surface elevation measured from the bottom of the grid;

566 p_0 = atmospheric pressure on the free surface;

567 $RRMSE$ = relative root mean square error;

568 S_0 = bed slope;

569 S_{ij} = strain rate tensor;

570 t = time;

571 u, v, w = flow velocity in the x, y, z direction;

572 U = dimensionless flow velocity;

573 V_F = volume fraction;

574 x_a = the lower limit of the zone;

575 x_b = the upper limit of the zone;

576 z = water level;

577 Δx, Δy, Δz = the grid size in the x, y, z direction;

578 α = water depth ratio;

579 β_h = percentage of the vertical velocity for a certain water depth;

580 β_p = depth-averaged percentage of the vertical velocity for a certain location;

581 $\bar{\beta}$ = average percentage of vertical velocity within the region;

582 ρ = fluid density;

583 μ_t = turbulence viscosity;

584 τ = bed shear stress;

585

586 Subscripts:

587 x, y, z = horizontal, transverse and vertical directions in the Cartesian coordinates;

588

589 **References**

590 Barnes, M.P., Baldock, T.E., 2006. Bed shear stress measurements in dam break and swash flows.
591 Proceedings of International Conference on Civil and Environmental Engineering. Hiroshima
592 University, Japan, 28–29 September.

593 Biscarini, C., Francesco S.D., Manciola P., 2010. CFD modelling approach for dam break flow
594 studies. Hydrol. Earth Syst. Sc. 14, 705-718, https://doi.org/10.5194/hess-14-705-2010.

595 Bristeau, M.O., Goutal, N., Sainte M.J., 2011. Numerical simulations of a non-hydrostatic shallow
596 water model. Comput. Fluids. 47, 51-64. https://doi.org/10.1016/j.compfluid.2011.02.013.

597 Bung, D.B., Hildebrandt, A., Oertel, M., Schlenkhoff, A., Schlurmann, T., 2008. Bore propagation
598 over a submerged horizontal plate by physical and numerical simulation. Proc. 31st Intl.Conf.
599 Coastal Eng., Hamburg, Germany, 3542–3553.

600 Cantero-Chinchilla F.N., Castro-Orgaz, O., Dey, S., Ayuso, J.L., 2016. Nonhydrostatic dam break
601 flows. I: physical equations and numerical schemes. J. Hydraul. Eng. 04016068.1-04016068.19,
602 https://doi.org/10.1061/(ASCE)HY.1943-7900.0001205.

603 Castro-Orgaz, O., Chanson, H., 2020. Undular and broken surges in dam-break flows: a review of
604 wave breaking strategies in a boussinesq-type framework. Environ, Fluid Mech. 154,
605 https://doi.org/0.1007/s10652-020-09749-3.

606 Chang, T.J., Kao, H.M., Chang, K.H., Hsu, M.H., 2011. Numerical simulation of shallow-water dam
607 break flows in open channels using smoothed particle hydrodynamics. J. Hydrol. 408, 78-90,
608 https://doi.org/10.1016/j.jhydrol.2011.07.023.

609 Chen, H.Y., Xu W.L., Deng, J., Xue,Y., Li, J., 2009. Experimental investigation of pressure load
610 exerted on a downstream dam by dam-break flow. J. Hydraul. Eng. 140, 199-207, https://doi.org/
611 10.1061/(ASCE)HY.1943-7900.0000743.
612 Favre H., 1935. Etude théorique et expérimentale des ondes de translation dans les canaux
613 découverts. Dunod, Paris. (in French).
614 Flow Science Inc., 2016. Flow-3D User's Manuals. Santa Fe NM.
615 Fraccarollo, L., Toro, E.F.. 1995. Experimental and numerical assessment of the shallow water model
616 for two-dimensional dam-break type problems. J. Hydraul. Res. 33(6), 843-864,
617 https://doi.org/10.1080/00221689509498555.
618 Guo, Y.K., Wu, X.G., Pan, C.H. Zhang, J.S., 2012. Numerical simulation of the tidal flow and
619 suspended sediment transport in the qiantang estuary. J Waterw. Port Coastal. 138, 192-202,
620 https://doi.org/10.1061/(ASCE)WW.1943-5460.0000118.
621 Guo, Y.K., Zhang, Z.Y. Shi, B., 2014. Numerical simulation of gravity current descending a slope
622 into a linearly stratified environment. J. Hydraulic Eng. 140, 04014061.1-04014061.10,
623 https://doi.org/10.1061/(ASCE)HY.1943-7900.0000936.
624 Khosronejad, A., Kang, S., Flora, K., 2019. Fully coupled free-surface flow and sediment transport
625 modelling of flash floods in a desert stream in the mojave desert, california. Hydrol. Process,
626 33(21), https://doi.org/10.1002/hyp.13527.
627 Khosronejad, A., Ghazian, M. A., Dionysios, A., Bagherizadeh, E., Flora, K., Farhadzadeh, A., 2020a.
628 A comparative study of rigid-lid and level-set methods for LES of open-channel flows:
629 morphodynamics. Environ. Fluid Mech. 145-164, https://doi.org/10.1007/s10652-019-09703-y.
630 Khosronejad, A., Flora, K., Zhang, Z.X., Kang, S., 2020b. Large-eddy simulation of flash flood

propagation and sediment transport in a dry-bed desert stream. Int. J. Sediment Res., 35(6),576-586, https://doi.org/10.1016/j.ijsrc.2020.02.002.

Khoshkonesh, A., Nsom, B., Gohari, S., Banejad, H., 2019. A comprehensive study of dam break over the dry and wet beds. Ocean Eng. 188, 106279.1-106279.18, https://doi.org/10.1016/j.oceaneng.2019.106279.

Kocaman, S., Ozmen-Cagatay, H., 2012. The effect of lateral channel contraction on dam break flows: laboratory experiment. J. Hydrol. 432-433, 145-153, https://doi.org/10.1016/j.jhydrol.2012.02.035.

Kocaman, S., Ozmen-Cagatay, H., 2015. Investigation of dam-break induced shock waves impact on a vertical wall. J. Hydrol. 525, 1-12. https://doi.org/10.1016/j.jhydrol.2015.03.040.

Larocque, L.A., Imran, J., Chaudhry, M.H., 2013a. Experimental and numerical investigations of two-dimensional dam-break flows. J. Hydraul. Eng. 139, 569-579, https://doi.org/10.1061/(ASCE)HY.1943-7900.0000705.

Larocque, L.A., Imran, J., Chaudhry, M.H., 2013b. 3D numerical simulation of partial breach dam-break flow using the LES and k-ε turbulence models. J. Hydraul. Res. 51, 145–157, https://doi.org/10.1080/00221686.2012.734862.

Lauber, G., Hager, W.H., 1998a. Experiments to dam break wave: horizontal channel. J. Hydraul. Res. 36, 291–307, https://doi.org/10.1080/00221689809498620.

Lauber, G., Hager, W.H., 1998b. Experiments to dam break wave: sloping channel. J. Hydraul. Res. 36, 761–773, https://doi.org/10.1080/00221689809498601.

Leal, J.G.A.B., Ferreira, R.M.L., Cardoso, A.H., 2006. Dam-break wave-front celerity. J. Hydraul. Eng. 132, 69–76, https://doi.org/10.1061/(ASCE)0733-9429(2006)132:1(69).

653 Liu, W.J., Wang, B., Guo, Y.K., Zhang, J.M., Chen, Y.L., 2020. Experimental investigation on the
654 effects of bed slope and tailwater on dam-break flows. J. Hydrol. 590, 125256,
655 https://doi.org/10.1016/j.jhydrol.2020.125256.
656 Marche, C., Beauchemin P. EL Kayloubi, A., 1995. Etude numérique et expérimentale des ondes
657 secondaires de Favre consécutives a la rupture d'un harrage. Can. J. Civil Eng. 22, 793-801, (in
658 French). https://doi.org/10.1139/l95-089.
659 Marra, D., Earl, T., Ancey, C., 2011. Experimental investigations of dam break flows down an
660 inclined channel. Proceedings of the 34th World Congress of the International Association for
661 Hydro-Environment Research and Engineering: 33rd Hydrology and Water Resources
662 Symposium and 10th Conference on Hydraulics in Water Engineering, Brisbane, Australia.
663 Marsooli, R., Wu, W., 2014. 3-D finite-volume model of dam-break flow over uneven beds based on
664 vof method. Adv. Water Resour. 70, 104-117. https://doi.org/10.1016/j.advwatres.2014.04.020.
665 Miller, S., Chaudhry, M.H., 1989. Dam-break flows in curved channel. J. Hydraul. Eng. 115,
666 1465-1478, https://doi.org/10.1061/(ASCE)0733-9429(1989)115:11(1465).
667 Mohapatra, P.K., Chaudhry, M.H., 2004. Numerical solution of Boussinesq equations to simulate
668 dam-break flows. J. Hydraul. Eng. 130, 156-159,
669 https://doi.org/10.1061/(ASCE)0733-9429(2004)130:2(156).
670 Oertel, M., Bung, D.B., 2012. Initial stage of two-dimensional dam-break waves: laboratory versus
671 VOF. J. Hydraul. Res. 50, 89-97. https://doi.org/10.1080/00221686.2011.639981.
672 Ozmen-Cagatay, H., Kocaman, S., 2012. Investigation of dam-break flow over abruptly contracting
673 channel with trapezoidal-shaped lateral obstacles. J. Fluids Eng. 134, 081204.
674 https://doi.org/10.1115/1.4007154.

675 Ozmen-Cagatay, H., Kocaman, S., Guzel, H., 2014. Investigation of dam-break flood waves in a dry
676 channel with a hump. J. Hydro-environ. Res. 8, 304-315,
677 https://doi.org/10.1016/j.jher.2014.01.005.
678 Park, I.R., Kim, K.S., Kim, J., Van, S.H., 2012. Numerical investigation of the effects of turbulence
679 intensity on dam-break flows. Ocean Eng. 42, 176-187,
680 https://doi.org/10.1016/j.oceaneng.2012.01.005.
681 Peregrine, D.H., 1966. Calculations of the development of an undular bore. J. Fluid Mech. 25,
682 321-330, 1966. https://doi.org/10.1017/S0022112066001678.
683 Savic Lj., Holly Jr, F.M., 1993. Dam break flood waves computed by modified Godunov method. J.
684 Hydraul. Res. 31, 187-204, https://doi.org/10.1080/00221689309498844.
685 Shigematsu, T., Liu, L.F., Oda, K., 2004. Numerical modeling of the initial stages of dam-break
686 waves. J. Hydraul. Res. 42, 183-195, https://doi.org/10.1080/00221686.2004.9628303.
687 Smagorinsky, J., 1963. General circulation experiments with the primitive equations. Part I: the basic
688 experiment. Mon. Weather Rev. 91, 99–164, https://doi.org/10.1126/science.27.693.594.
689 Soares-Frazao, S., Zech Y., 2002. Undular bores and secondary waves - Experiments and hybrid
690 finite-volume modeling. J. Hydraul. Res. 40, 33-43, https://doi.org/10.1080/00221680209499871.
691 Stansby, P. K., Chegini, A., Barnes, T.C.D., 1998. The initial stages of dam-break flow. J. Fluid Mech.
692 370, 203-220. https://doi.org/10.1017/022112098001918.
693 Treske, A., 1994. Undular bores (favre-waves) in open channels - experimental studies. J. Hydraul.
694 Res. 32, 355-370. https://doi.org/10.1080/00221689409498738.
695 Wang, B., Chen, Y.L., Wu, C., Dong, J.H., Ma, X., Song, J.J., 2016. A semi-analytical approach for
696 predicting peak discharge of floods caused by embankment dam failures. Hydrol. Process, 30,

https://doi.org/10.1002/hyp.10896.

Wang, B., Chen, Y.L, Wu, C., Peng,Y., Ma, X., Song, J.J., 2017. Analytical solution of dam-break flood wave propagation in a dry sloped channel with an irregular-shaped cross-section. J. Hydro-environ. Res. 14, 93–104, https://doi.org/10.1016/j.jher.2016.11.003.

Wang, B., Chen, Y.L, Wu, C., Peng, Y., Song, J.J., Liu, W.J., Liu, X., 2018. Empirical and semi-analytical models for predicting peak outflows caused by embankment dam failures. J. Hydrol. 562, 692–702. https://doi.org/10.1016/j.jhydrol.2018.05.049.

Wang, B., Zhang, J.M., Chen, Y.L., Peng, Y., Liu, X., Liu, W. J., 2019. Comparison of measured dam-break flood waves in triangular and rectangular channels. J. Hydrol. 575, 690-703. https://doi.org/10.1016/j.jhydrol.2019.05.081.

Wang, B., Liu, W.J., Zhang, J.M., Chen, Y.L., Wu, C., Peng, Y., Wu Z.Y., Liu, X., Yang, S., 2020a. Enhancement of semi-theoretical models for predicting peak discharges in breached embankment dams. Environ Fluid Mech. 12, https://doi.org/10.1007/s10652-019-09730-9.

Wang, B., Chen, Y.L., Peng, Y., Zhang, J.M., Guo, Y.K., 2020b. Analytical solution of shallow water equations for ideal dam-break flood along a wet bed slope. J. Hydraul. Eng. 146, 06019020.1-06019020.6, https://doi.org/10.1061/(ASCE)HY.1943-7900.0001683.

Wang, B., Liu, W.J., Wang, W., Zhang, J.M., Chen, Y.L., Peng, Y., Liu, X., Yang, S., 2020c. Experimental and numerical investigations of similarity for dam-break flows on wet bed. J. Hydrol. 583, 124598, https://doi.org/10.1016/j.jhydrol.2020.124598.

Wang, B., Liu, X., Zhang, J.M., Guo, Y.K., Chen, Y.L., Peng, Y., Liu, W.J., Yang, S., Zhang, F.J., 2020d. Analytical and experimental investigations of dam-break flows in triangular channels with wet-bed conditions. J. Hydraul. Eng. 146, 04020070,

https://doi.org/10.1061/(ASCE)HY.1943-7900.0001808.

Wu, W.M, Wang, S., 2007. One-dimensional modeling of dam-break flow over movable beds. J. Hydraul. Eng., 133(1), 48-58. https://doi.org/10.1061/(ASCE)0733-9429(2007)133:1(48).

Xia, J., Lin, B., Falconer, R. A., Wang, G., 2009. Modelling dam-break flows over mobile beds using a 2d coupled approach. Adv. Water Resour. 33, 171-183, https://doi.org/10.1016/j.advwatres.2009.11.004.

Yang, S.L., Yang, W.L., Qin, S.Q., Li, Q., Yang, B., 2018a. Numerical study on characteristics of dam-break wave. Ocean Eng. 159, 358-371, https://doi.org/10.1016/j.oceaneng.2018.04.011.

Yang, S.L., Yang, W.L., Qin, S.Q., Li, Q., 2018b. Comparative study on calculation methods of dam-break wave. J. Hydraul. Res. 1-13, https://doi.org/10.1080/00221686.2018.1494057.

Tab. captions list

Fig. captions list

743 profile; (c) variation of the bed shear stress; (d) error value of the bed shear stress.

744 Fig. 7. Schematic diagram of regional division.

745 Fig. 8. Variation of water surface profile (a) α = 0.1; (b) α = 0.3; (c) α = 0.5; (d) α = 0.7.

746 Fig. 9. Froude number for α = 0.1 (a) variation with time; (b) variation with wavefront position.

747 Fig. 10. Characteristics of velocity distribution (a) α = 0.1; (b) α = 0.3; (c) α = 0.5; (d) α = 0.7.

748 Fig. 11. Average proportion of the vertical velocity (a) α = 0.1; (b) α = 0.3; (c) α = 0.5; (d) α = 0.7.

749 Fig. 12. Bed shear stress distribution (a) α = 0.1; (b) α = 0.3; (c) α = 0.5; (d) α = 0.7.

750 Fig. 13. Variation of the maximum bed shear stress position with time (a) α = 0.1; (b) α = 0.3; (c) α =
751 0.5; (d) α = 0.7.

752 Fig. 14. Time when the maximum bed shear stress appears at different positions (a) α = 0.1; (b) α =
753 0.3; (c) α = 0.5; (d) α = 0.7.

754 Fig. 15. Movement characteristics of the fluid particles (a) α = 0.1; (b) α = 0.3; (c) α = 0.5; (d) α =
755 0.7.